UNIVERSITY OF AMSTERDAM

UvA-DARE (Digital Academic Repository)

Probing the electronic structure at the boundary of topological insulators in the Bi_2Se_3 family by combined scanning tunneling and atomic force microscopy

Setescak, Christoph S.; Aguilera, Irene; Weindl, Adrian; Kronseder, Matthias; Donarini, Andrea; Giessibl, Franz J.

DOI
10.1103/PhysRevB.111.165305

Publication date
2025

Document Version
Final published version

Published in
Physical Review B

License
Article 25fa Dutch Copyright Act (https://www.openaccess.nl/en/policies/open-access-in-dutch-copyright-law-taverne-amendment)

Link to publication

Citation for published version (APA):
Setescak, C. S., Aguilera, I., Weindl, A., Kronseder, M., Donarini, A., & Giessibl, F. J. (2025). Probing the electronic structure at the boundary of topological insulators in the Bi_2Se_3 family by combined scanning tunneling and atomic force microscopy. *Physical Review B*, *111*(16), Article 165305. https://doi.org/10.1103/PhysRevB.111.165305

General rights
It is not permitted to download or to forward/distribute the text or part of it without the consent of the author(s) and/or copyright holder(s), other than for strictly personal, individual use, unless the work is under an open content license (like Creative Commons).

Disclaimer/Complaints regulations
If you believe that digital publication of certain material infringes any of your rights or (privacy) interests, please let the Library know, stating your reasons. In case of a legitimate complaint, the Library will make the material inaccessible and/or remove it from the website. Please Ask the Library: https://uba.uva.nl/en/contact, or a letter to: Library of the University of Amsterdam, Secretariat, P.O. Box 19185, 1000 GD Amsterdam, The Netherlands. You will be contacted as soon as possible.

UvA-DARE is a service provided by the library of the University of Amsterdam (https://dare.uva.nl)

Download date:10 Oct 2026

Editors' Suggestion

Probing the electronic structure at the boundary of topological insulators in the Bi_2Se_3 family by combined scanning tunneling and atomic force microscopy

Christoph S. Setescak [1,*] Irene Aguilera [2] Adrian Weindl [1] Matthias Kronseder [1] Andrea Donarini [3] and Franz J. Giessibl [1]

[1] *Institute of Experimental and Applied Physics, University of Regensburg, Universitätstraße 31, 93053 Regensburg, Germany*

[2] *Institute for Theoretical Physics, University of Amsterdam and European Theoretical Spectroscopy Facility (ETSF), Science Park 904, 1098 XH Amsterdam, Netherlands*

[3] *Institute of Theoretical Physics, University of Regensburg, Universitätstraße 31, 93053 Regensburg, Germany*

(Received 21 November 2024; revised 21 February 2025; accepted 31 March 2025; published 28 April 2025)

We develop a numerical scheme for the calculation of tunneling current I and differential conductance $\mathrm{d}I/\mathrm{d}V$ of metal- and CO-terminated STM tips on the topological insulators Bi_2Se_3, Bi_2Te_2Se as well as Bi_2Te_3, and find excellent agreement with experiment. The calculation is an application of Chen's derivative rule, whereby the Bloch functions are obtained from Wannier-interpolated tight-binding Hamiltonians and maximally localized Wannier functions from first-principle DFT+GW calculations. We observe signatures of the topological boundary modes, their hybridization with bulk bands, Van Hove singularities of the bulk bands, and characterize the orbital character of these electronic modes using the high spatial resolution of STM and AFM. Bare DFT calculations are insufficient to explain the experimental data, which are instead accurately reproduced by many-body-corrected GW calculations.

DOI: 10.1103/PhysRevB.111.165305

I. INTRODUCTION

Solid-state physics seeks to understand the large-scale properties of materials, in principle deducing them from atomic-scale behavior. In insulators, the atomic arrangement and electron-electron interaction result in bulk valence and conduction bands that are separated by an energy gap. These bands are classified using topological invariants, which define distinct topological phases of matter [1–4]. In three-dimensional topological insulators, nontrivial invariants give rise to gapless boundary modes, linking atomic-scale behavior to emergent large-scale phenomena. These boundary modes are characterized by spin-polarized, nearly linear dispersion relations, thus effectively describing massless particles.

Prototypical examples of three-dimensional topological insulators include materials from the Bi_2Se_3 family, such as Bi_2Se_3, Bi_2Te_2Se, and Bi_2Te_3. The dispersion relation of topological insulators can be very well studied using angle-resolved photoemission spectroscopy (ARPES) [5]. However, standard ARPES is only able to probe occupied states and more advanced time-resolved ARPES (trARPES) or two-photon ARPES are necessary to probe unoccupied states [5]. Furthermore, ARPES is limited to momentum space and to length scales much larger than atomic ones. Transport and ferromagnetic resonance experiments have demonstrated that atomic-scale defects have a large influence on sample properties [6–8].

To overcome these limitations and explore atomic-scale phenomena in real space, scanning probe microscopy techniques, such as scanning tunneling microscopy (STM), atomic force microscopy (AFM), and scanning tunneling spectroscopy (STS), are helpful [9].

Examples of previous scanning probe studies on materials in the Bi_2Se_3 family are plentiful [10–12]. The influence of native point defects on the local density of states (LDOS) in Bi_2Te_3 has been documented in Ref. [13] and impurity resonances in Bi_2Se_3 have been studied in Ref. [14]. Furthermore, it is possible to identify the doping character of native point defects [13,15], which can also be probed directly via AFM [16]. Scattering at step edges on Bi_2Te_3 has been used in Ref. [17] to quantify the dispersion and verify the spin polarization of the topological boundary mode. In Refs. [18–20] changes in the LDOS close to few-atomic steps on Bi_2Se_3 have been studied, which indicate increased conductance in the energy range of the topological boundary mode close to the step edge. The necessity of quantitatively accurate calculations of the $\mathrm{d}I/\mathrm{d}V$ signal becomes apparent from this study, as such changes can be caused and explained by changes in the local work function and chemical potential close to step edges. This is in contrast with other possible explanations, such as additional one-dimensional electronic states. Further, recent theoretical studies propose atomic-scale experiments that would use ring states at defects as a probe for bulk topological properties [21].

In this article, we wish to establish how the band structure of these materials can be studied using experimental techniques that access the atomic scale. Experimental results presented here include measurements of the $\mathrm{d}I/\mathrm{d}V$ signal over a bias range where characterizing bulk energy levels is possible. Furthermore, we probe the $\mathrm{d}I/\mathrm{d}V$ signal throughout the valence and conduction bands with atomic resolution,

*Contact author: Christoph.Setescak@physik.uni-regensburg.de

 ©2025 American Physical Society

giving us a grip on characterizing the orbital character of the Bloch bands.

State-of-the-art *GW* calculations are used to construct tight-binding Hamiltonians for thick slab geometries and are the basis for calculating the differential conductance $\mathrm{d}I/\mathrm{d}V$ through the atomic-scale tip-sample junction. Because of the large sample geometries in our experiment, i.e., semi-infinite single crystals or thick slabs, it is not feasible to study these directly with *GW* or DFT, necessitating the use of tight-binding (TB) Hamiltonians. Employing *GW* calculations is an improvement over previous studies, as it has been shown that bare DFT calculations are not sufficient to accurately describe this material class [22]. In our calculation, we include the energy dependence of the $\mathrm{d}I/\mathrm{d}V$ signal as well as the dependence on the position of the tip apex $\mathbf{r}_0$.

The paper is organized as follows. In Sec. II, we give an overview of our findings and review relevant literature. Our methods are described in detail in Sec. III. The results of scanning tunneling spectroscopy on the three compounds are in Sec. IV. Section V demonstrates how these results can be applied to probe the influence of many-body corrections on the band structure. Section VI reports how the orbital character of the band structure can be probed using our experimental setup. Our conclusions are summarized in Sec. VII

II. OVERVIEW AND COMPARISON TO PREVIOUS RESULTS

Figure 1 shows the main result of this article. Panels 1(a)–1(c) display in orange $\mathrm{d}I/\mathrm{d}V$ spectra measured with CO-terminated tips on the surfaces of Bi_2Se_3, Bi_2Te_2Se, and Bi_2Te_3, alongside the calculated $\mathrm{d}I/\mathrm{d}V$ spectra in blue. The corresponding half-space band structures are presented in Figs. 1(d)–1(f). Here, the color bar indicates the projection of the states onto the Wannier functions associated with the atoms of the topmost quintuple layer (QL), with bulk bands appearing in light blue and surface states shown as dark purple lines.

(i) Our numerical scheme for calculating the $\mathrm{d}I/\mathrm{d}V$ spectra can be summarized in five steps. The starting point is Wannier-interpolated TB Hamiltonians for materials in the Bi_2Se_3 family derived from many-body renormalized *GW* calculations [22]. From these we construct half-space Hamiltonians using Dirichlet boundary conditions. We represent the Bloch functions in real-space using maximally localized Wannier functions [23]. Propagation of the Bloch functions into the tip-sample junction is modeled under the assumption of noninteracting electrons traveling in a laterally averaged potential. Eventually, the electron tunneling into and out of the metal and CO-terminated tips is calculated using Chen's derivative rule [24,25].

(ii) Metal tips are typically preferred for $\mathrm{d}I/\mathrm{d}V$ measurements. They have a simpler apex electronic structure dominated by an *s*-wave orbital, whereas a linear combination of *s*- and *p*-wave orbitals is necessary to properly describe CO-terminated tips. With the calculation method presented in Sec. III and in particular Sec. III C, it is possible to accurately model the tunneling matrix element into a mix of tip orbitals. This increased complexity of the CO-terminated tip in STS experiments is outweighed, though, by their very high chemical stability and high spatial resolution, as demonstrated, for example, in Sec. VI B and Refs. [26–28]. For a better comparison to existing literature, we also show the spectrum of a metal tip on the surface of Bi_2Se_3 in Sec. IV A.

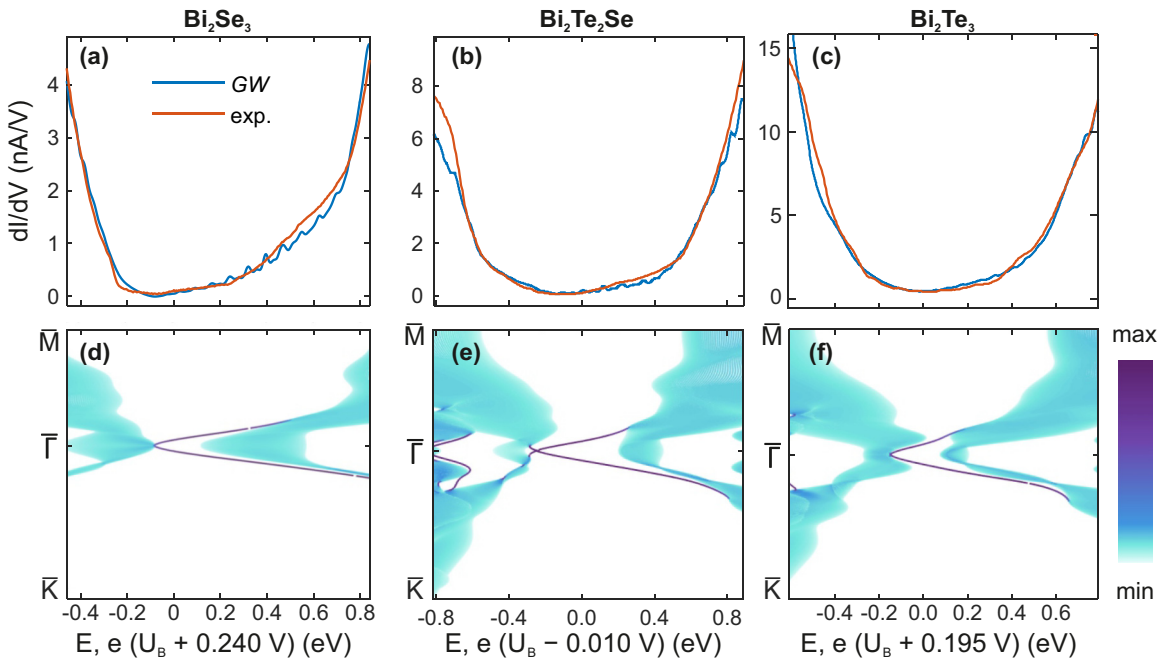

FIG. 1. Comparison of simulated and experimental $\mathrm{d}I/\mathrm{d}V$ spectrum of CO-functionalized tips on the (a) surface of Bi_2Se_3, (b) surface of Bi_2Te_2Se, and (c) surface of Bi_2Te_3. The half-space band structures are plotted in (d)–(f). The energy axes for each compound are identical and are related to the bias voltage by a shift, owing to defects doping the crystal. The color scale in (d)–(f) indicates the fraction of the eigenstate in the first quintuple layer.

(iii) Throughout the article we give the energy E relative to the calculated Fermi level [22]. Because of defects in crystal samples, the experimental Fermi level is shifted by ΔE_F. The experimental counterpart of the energy E is the bias voltage U_B. To facilitate a comparison between experiment and theory via the plots, we shift the bias voltage U_B by ΔE_F. The magnitude of ΔE_F is a measure for the level of unintentional doping in the crystals.

(iv) The general shape of the $\mathrm{d}I/\mathrm{d}V$ spectrum is similar across the three compounds, as can be seen in Figs. 1(a)–1(c). In the region close to the bulk band gap, the differential conductance is greatly reduced. Here, we see linear relations between the $\mathrm{d}I/\mathrm{d}V$ signal and bias voltage U_B. Towards the bulk bands the $\mathrm{d}I/\mathrm{d}V$ signal increases rapidly. We find excellent agreement between experiment and theory and give an overview of the findings in the remainder of this section. A more detailed discussion follows in Secs. IV, V, and VI.

(v) The emergence of the gap-closing boundary mode upon restricting the system to half-space has been studied since the first band structure calculations of three dimensional topological insulators, published in Ref. [29]. The signature of this boundary mode in the $\mathrm{d}I/\mathrm{d}V$ spectrum is a linear increase of the differential conductance inside the bulk band gap. Focusing on the compound Bi_2Se_3, this linear increase can be seen in the experimental data and calculation in Fig. 1(a) for $-0.2\,\mathrm{eV} < E < 0.23\,\mathrm{eV}$. For a single band with index n and dispersion relation $E_n(\mathbf{k})$, the partial density of states is given as

$$\begin{aligned}\mathrm{DOS_n}(\mathbf{r},\mathrm{E}) &= \frac{1}{(2\pi)^2}\int_{\mathrm{BZ}} \delta(E - E_n(\mathbf{k}))\,\mathrm{d}k_x\mathrm{d}k_y \\ &= \frac{1}{(2\pi)^2}\int_{\mathrm{CEC_n(E)}} \|\mathrm{grad}(E_n)(\mathbf{k})\|^{-1}\,\mathrm{dS}. \end{aligned} \quad (1)$$

Here, $\mathrm{CEC}_n(E)$ is the constant energy contour of the boundary mode n at energy E, i.e., the curve consisting of all $\mathbf{k} \in \mathrm{BZ}$ with $E_n(\mathbf{k}) = E$. For a linear and isotropic dispersion relation, we have $\|\mathrm{grad}(E_n)(\mathbf{k})\| = \hbar v_F$, where v_F is a constant referred to as the Fermi velocity [30]. The constant energy contour $\mathrm{CEC_n(E)}$ of such a topological boundary mode is circular and the line integral in Eq. (1) can be evaluated to be

$$\mathrm{DOS}_n(\mathbf{r}, E) = \frac{|E - E_D|}{2\pi\hbar^2 v_F^2}, \quad (2)$$

where E_D is the energy of the Dirac point. This result follows from calculating the circumference of the $\mathrm{CEC}_n(E)$, which is equal to $\frac{2\pi}{\hbar v_F}|E - E_D|$. The differential conductance $\mathrm{d}I/\mathrm{d}V$ is closely related to the DOS, and thus from Eq. (2) it becomes clear that we expect a linear increase of the $\mathrm{d}I/\mathrm{d}V$ signal away from the Dirac point within the band gap. This linear section is reproduced by the more involved quantitative calculation introduced in Sec. III. We note that this key signature of topological boundary modes can also be explained by the simplified tight-binding model described in Refs. [29,31], which only considers four electronic degrees of freedom.

(vi) In previous literature effective, low-energy tight-binding models have been presented, which reproduce the dispersion of the bands closest to E_F in the vicinity of Γ [29,32]. However, these are not sufficient to properly describe our experimental results. To correctly describe our experimental observations it is necessary to consider bulk and surface electronic modes, as well as surface resonances. A strength of our numerical approach is its ability to describe the surface resonances accurately without relying on any free parameter. The resonance of the boundary mode of Bi_2Se_3 with the bulk valence band edge is of particular interest. From Figs. 1(a) and 1(d), it can be deduced that the minimum of the $\mathrm{d}I/\mathrm{d}V$ spectrum on Bi_2Se_3 corresponds to the Dirac point, which agrees with previous studies [12,18]. The linear increase in differential conductance away from the Dirac point ($E_D = -0.14\,\mathrm{eV}$), as shown in Fig. 1(a), was attributed to contributions from the upper and lower halves of the Dirac cone [18]. This would be a fitting interpretation if Bi_2Se_3 were a topological insulator (with a possibly indirect bulk band gap) with the Dirac point isolated from the bulk bands. However, the *GW* calculations, ARPES, and magneto-optical measurements [33,34] show that Bi_2Se_3 is a direct band gap semiconductor and the Dirac point coincides with the valence band maximum (VBM) at the Γ point, as displayed in Fig. 1(d). Nonetheless, our calculation—the blue curve in Fig. 1(a)—shows that this linear section in the $\mathrm{d}I/\mathrm{d}V$ spectrum can be explained by tunneling into the bulk valence bands. Thus, the attribution of the linear increase in the differential conductance for $E < E_D$ to a lower half of the Dirac cone has to be modified. This is of great importance if one is interested in studying a gap opening in the topological boundary mode [35]. The situation is analogous for metal tips, a detailed treatment of which is given in Sec. IV A.

(vii) In our experiment, we also find signatures that allow for the investigation of the bulk bands. We observe that the bulk modes near the conduction band edge contribute minimally to the $\mathrm{d}I/\mathrm{d}V$ signal, as the tunneling matrix element for states close to the conduction band edge is significantly suppressed. This suppression is clearly shown for the three compounds in Sec. IV. In the $\mathrm{d}I/\mathrm{d}V$ spectrum measured on the surface of Bi_2Se_3, shown in Fig. 1(a), sharp increases are observed at $E = -0.23\,\mathrm{eV}$ and $E = 0.72\,\mathrm{eV}$. These energies correspond to a flattening of the dispersion relation in the $\bar{\Gamma}$–$\bar{\mathrm{M}}$ direction, visible in Fig. 1(d). Similar observations can be made for Bi_2Te_2Se and Bi_2Te_3. A quantitatively correct tight-binding model that reproduces first-principle calculations over the entire Brillouin zone and an extended energy range is necessary. Such models, which reproduce DFT-band structures have been already calculated in Ref. [29] and Slater-Koster parameters were published in Ref. [36] for Bi_2Se_3 and Bi_2Te_3. However, regardless of the surface resonances, we find that standard DFT calculations are not sufficient to correctly describe the overall features of the experimental observations. Rather, many-body corrections are necessary: The flattening of the dispersion relation is in fact closely related to the size of the trivial band gaps at the Brillouin zone boundary and the size of these gaps is strongly influenced by the *GW* correction [22]. Our experimental observations are explained accurately by the *GW* corrected TB Hamiltonians. A comparison between the *GW* corrected TB Hamiltonians and the TB Hamiltonians without many-body correction for Bi_2Se_3 is given in Sec. V. Thus, we demonstrate that not only are the drastic changes in the band structure near Γ, induced by the *GW* correction, consistent with experimental observations,

but the values of the trivial band gaps far from the Γ point also align more closely with the *GW* calculations.

(viii) Arguably the compound Bi_2Te_2Se comes closest to the idealized notion of three-dimensional topological insulators, put forth by effective TB models such as in Ref. [29]. For one, it is an indirect semiconductor and the Dirac point lies below the VBM, evident from Fig. 1(e). Furthermore, it displays a large bulk band gap, and thus the topological boundary mode is separate from the bulk bands over a large energy range. The experimental and calculated $\mathrm{d}I/\mathrm{d}V$ spectrum are plotted in Fig. 1(b). The bulk band gap and thus also the energy range on which an isolated Dirac cone can be observed is on the order of 0.37 eV, much larger for Bi_2Te_2Se than for Bi_2Se_3 and Bi_2Te_3, as can be seen in the half-space band structure, which is plotted in Fig. 1(e). In Sec. IV B, we discuss the $\mathrm{d}I/\mathrm{d}V$ spectrum of a CO-terminated tip on the surface of Bi_2Te_2Se with focus on the energy range around the bulk band gap.

(ix) Furthermore, a desirable property of the ternary compound is its much smaller level of bulk doping, compared to the binary compounds studied in this article. This is in part owing to the presence of both hole- and electron-producing defects [7,8,37]. In our study, we detected slight *n* doping or slight *p* doping after cleaving the Bi_2Te_2Se sample in the UHV chamber. Figure 1(b) shows that the chemical potential is shifted by $\Delta E_F = -10$ meV relative to the calculated Fermi level, while Fig. 5 in Sec. IV B presents a spectrum from a different location on the sample, revealing a shift of $\Delta E_F = 10$ meV. Such spatial variations are in agreement with previous studies of the surface potential fluctuations on this material class [6,8]. The position of the Fermi level is of vital importance in transport measurements. Our experiments are not significantly affected by the slight *n* doping, or even *p* doping, as we can probe unoccupied as well as occupied states. This is in contrast to ARPES experiments, where additional dopants have to be added to the surface in order to tune the energetic position of the Dirac point [38] or, alternatively, trARPES has to be used. To first approximation, a shift in the chemical potential leads to a shift of the entire band structure [11]. But, strictly speaking, because of the screening of the electron-electron interaction, the position of the chemical potential does influence the band profile [39]. As the first-principles calculations for Bi_2Se_3 and Bi_2Te_3 do not consider shifts in the chemical potential owing to dopants, there is a small error. However, for Bi_2Te_2Se, the shift in the chemical potential is minimal, and overall we see a similar level of agreement between experiment and theory. Thus we can conclude that this effect is minimal, for the systems studied in this paper.

(x) With AFM, we observe a large number of substitutional defects in the first atomic layer of Bi_2Te_2Se. Presumably, these are because of the chemical and physical similarities of Te and Se. We position the tip as far away from these substitutional defects as possible for all the measurements presented on Bi_2Te_2Se in this article.

(xi) Because of the very small bulk band gap of Bi_2Te_3, the linear section in the $\mathrm{d}I/\mathrm{d}V$ spectrum shown in Fig. 1(c) is hard to identify. The half-space band structure computed with the *GW* Hamiltonian and plotted in Fig. 1(f) indicates that an isolated Dirac cone exists only for an energy range of 0.07 eV, with the lower part of the Dirac cone covered by the bulk valence bands. As a result of the smaller bulk band gap, the onset of the bulk bands is energetically much closer together than for the other two compounds. The Bi_2Te_3 sample was prepared by molecular-beam epitaxy (MBE) and consists of 7 quintuple layers, which in previous work has been shown to be sufficient for compounds in this material class to behave bulk like [40]. On the MBE sample, we observe an elevated defect density compared to samples cleaved from single crystals of Bi_2Se_3 [16]. The sample preparation processes are described in the Supplemental Material [41] and Refs. [42,43].

(xii) In previous studies [10,12,15,44], a similar comparison between experimental and calculated $\mathrm{d}I/\mathrm{d}V$ spectra on these compounds was attempted using pure first-principles calculations. The drawback of a full first-principles calculation is that the integration over the Brillouin zone can only be carried out on a very coarse grid of crystal momenta, because of the high computational cost. In particular, a 24×24 Monkhorst-Pack grid was used in Ref. [15]. Here, owing to the low computational burden of the tight-binding model, we can perform the integration on a grid of 80×80 crystal momenta in the surface Brillouin zone on a personal computer with 64 GB of RAM using a MATLAB implementation [45]. The result is numerical artefacts are virtually eliminated in the calculation of the $\mathrm{d}I/\mathrm{d}V$ spectra, while we use physically realistic smoothing parameters. A drawback of our method is we do not consider surface effects self-consistently. However, we believe that the comprehensive agreement between experiment and theory justifies *a posteriori* our approach.

(xiii) For Bi_2Te_3 we present in Sec. IV C $\mathrm{d}I/\mathrm{d}V$ spectroscopy over a large bias range of $U_B \in [-2\,\mathrm{V},\ 2\,\mathrm{V}]$. *A priori* we did not expect that it would be possible to reproduce this experimental result with the precision demonstrated in Fig. 3 of Sec. IV C. During the analysis of this data, we explain how Van Hove singularities owing to a flat dispersion of electronic modes at the Brillouin zone boundary lead to the emergence of characteristic peaks in the $\mathrm{d}I/\mathrm{d}V$ spectra. In the past, one hurdle regarding the interpretation of $\mathrm{d}I/\mathrm{d}V$ spectra has been their sometimes feature-less U-shaped appearance. Our result introduces a means to circumvent this problem for a more rigorous analysis. In Sec. V, we use comparable $\mathrm{d}I/\mathrm{d}V$ spectra on Bi_2Se_3 to explain that the experimental observation aligns with the *GW* calculation, whereas pure DFT falls short of reproducing experimental data. Another application is given in Sec. VI A, at the example of Bi_2Te_3. By measuring $\mathrm{d}I/\mathrm{d}V$ spectra within $-2\,\mathrm{V} < U_B < 2\,\mathrm{V}$ above both Te atoms and hollow sites on the Bi_2Te_3 surface, the orbital character of the Bloch bands can be investigated.

III. METHODS

A. First-principles methods

The first-principles calculations were performed with density functional theory (DFT) and the *GW* method with the schemes and convergence parameters discussed in Ref. [22]. The results are based on the all-electron full-potential augmented plane-wave (FLAPW) formalism, as implemented in the DFT code FLEUR [46] and the *GW* code SPEX [47]. For the *GW* calculations, the spin-orbit coupling was

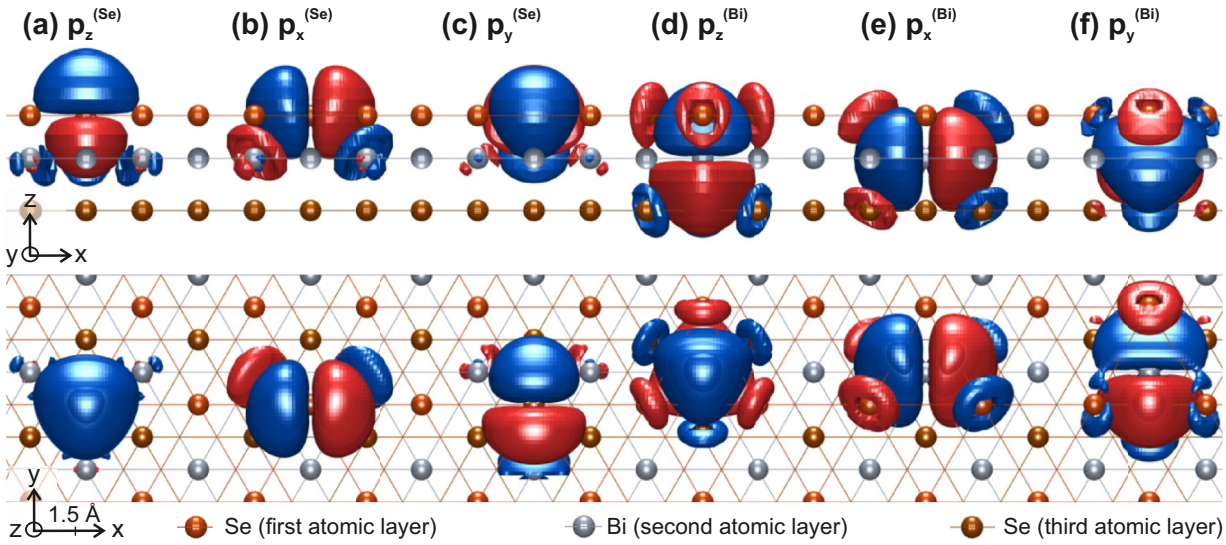

FIG. 2. Positive (red) and negative (blue) isosurfaces of the Wannier functions of Bi_2Se_3 localized on the selenium and bismuth atoms in the first and second atomic layers. Orthographic projection onto z-x plane in the top row and onto y-x plane in the bottom row. The band structure close to E_F is dominated by Wannier functions with p_x, p_y, and p_z orbital character, such that the Wannier functions above are sufficient for the calculations in this paper. The Wannier functions localized on the Se atoms (light orange) extend further into the van der Waals gap than those localized on the Bi atoms (grey).

included in the mean-field starting point, following the approach of Ref. [48].

The *GW* approximation includes renormalization effects owing to electron-electron interaction contributions that are neglected in DFT. *GW* has consistently shown improved results compared to DFT in the theoretical description of this family of materials. This includes a variety of properties such as critical points of topological phase transitions [35]; band gaps, effective masses, and spin-orbit splittings [33,48–50]; the direct or indirect nature of the band gap [33,49]; orbital contributions [51]; optical properties [52,53]; EELS [54]; dispersion of the topological surface states [22]; and electron dynamics [55].

After the DFT and *GW* calculations, we constructed tight-binding (TB) Hamiltonians whose parameters are obtained fully from first-principles with the help of Wannier functions. Wannier functions are linear combinations of Bloch eigenfunctions and are defined in such a way that they are maximally spatially localized. To obtain the maximally localized Wannier functions (shown in Fig. 2), we used the Wannier90 library [56] embedded in the SPEX code. These Wannier functions form the basis in which the TB Hamiltonian is expressed. Wannier functions constitute a more natural and more accurate basis for TB Hamiltonians of solids than pure atomic orbitals. We adopted the standard one-shot (perturbative) *GW* approximation in which the DFT energies are corrected but not the associated wavefunctions. Thus, the Wannier basis functions are calculated based on DFT and used for both Hamiltonians [57].

The construction of the TB parameters fully from first principles is done using the so-called Wannier interpolation technique. A formal description of Wannier interpolation can be found in Ref. [23]. The basic idea is as follows: The actual first-principles calculation of the DFT or *GW* Hamiltonian is carried out on a coarse uniform $\mathbf{k}$ mesh. A set of selected bands is then transformed into maximally localized Wannier functions. The Hamiltonian is now expressed in real space in a basis of these Wannier functions. Thanks to the spatial localization of the Wannier functions, long-ranged interactions can be truncated, allowing for an inverse Fourier transformation to provide the Hamiltonian at an arbitrary $\mathbf{k}$ point. This is called the "interpolated" Hamiltonian and very often gives rise to physical and surprisingly accurate band structures, which are practically indistinguishable from those obtained in an explicit first-principles calculation.

As we showed in Ref. [22], these bulk Hamiltonians in real space can also be used to construct film Hamiltonians that provide exceptional accuracy in the description of bulk and surface states of this family of materials.

B. Calculation of Bloch functions

Mathematically, the interpolated TB Hamiltonian is a map that assigns to any $\mathbf{k}$ in the bulk Brillouin zone BZ a matrix acting on the electronic degrees of freedom,

$$\begin{aligned} \widehat{\mathrm{H}}&:\mathrm{BZ} \longrightarrow \mathrm{Mat}(30;\mathbb{C}) \\ \mathbf{k} &\longmapsto \widehat{\mathrm{H}}(\mathbf{k}) = \sum_{\mathbf{R}\in\mathcal{L}} \mathrm{H}_{\mathbf{R}}\, \mathrm{e}^{\mathrm{i}\mathbf{k}\cdot\mathbf{R}}. \end{aligned} \tag{3}$$

Here, $\mathcal{L}$ denotes the set of all lattice vectors and the hopping matrices $\mathrm{H}_{\mathbf{R}}$ are obtained fully from first principles as discussed in Sec. III A and given in the Supplemental Material of Ref. [22]. The basis functions, corresponding to the indices of the hopping matrices $\mathrm{H}_{\mathbf{R}}$, are the following: given by the p orbitals $p_\alpha^{i\sigma}$ and ordered respectively according to the spin $\sigma = \uparrow, \downarrow$, to the atom number $i = 1, \ldots, 5$ on which the basis function is localized and to their spatial orientation $\alpha = z, x, y$. A selection of these orbitals is depicted in Fig. 2.

The s bands are energetically well separated from the p bands, such that the orbitals given above are sufficient for a description of the band structure close to E_F [22]. We note that the Hamiltonian in Eq. (3) is in the so-called *lattice gauge*. The procedure to obtain $\mathrm{H}_{\mathbf{R}}$ can be performed after the DFT calculation or after the *GW* correction. When including many-body effects, the Hamiltonian, or more precisely the self-energy operator, is not necessarily self-adjoint, as it contains the lifetime of quasiparticle states. In this paper we only consider real eigenvalues of the many-body corrected TB Hamiltonians.

In the lattice gauge, the Bloch functions can be written as a linear combination of the Wannier functions $w_\nu(\mathbf{r})$,

$$\Psi_{n,\mathbf{k}}(\mathbf{r}) = \sum_{\nu\in I} \mathcal{C}^n_\nu(\mathbf{k}) \sum_{\mathbf{R}\in\mathcal{L}} e^{i\mathbf{k}\cdot\mathbf{r}} w_\nu(\mathbf{r}-\mathbf{R}), \tag{4}$$

where $\mathcal{C}^n(\mathbf{k})$ is the n-th eigenvector of the matrix $\widehat{\mathrm{H}}(\mathbf{k})$ and we denote by I the index set labeling the spin, orbital, and atomic site. With Eqs. (3) and (4) it is possible to analyze the bulk electronic properties, for example, as done in Fig. 7 in Sec. V of this article. The Wannier functions $w_\nu(\mathbf{r})$ are obtained from first-principles as described in Sec. III A and shown in Fig. 2.

To interpret the spectroscopic measurements presented in this article, the electronic structure of half-space or thick film systems is relevant. In this case, the system size is so large that it cannot be studied by *GW* or DFT anymore. With the hopping matrices $\mathrm{H}_{\mathbf{R}}$, it is possible to construct the TB Hamiltonian of samples with different geometries, by constructing the Hamiltonian as block matrix indexed by the lattice sites $\mathbf{R}_i$ and placing $\mathrm{H}_{\mathbf{R}}$ wherever $\mathbf{R}_i - \mathbf{R}_j = \mathbf{R}$. In the case of a film system with a layered structure, we maintain translational symmetry parallel to the sample surface. Thus, the Hamiltonian in this case is a block matrix populated close to the diagonal. The block entries are still dependent on the momentum $\mathbf{k}_\parallel$ parallel to the surface. In this picture, the on-diagonal terms correspond to intralayer terms, whereas the off-diagonal entries correspond to interlayer terms. Alternatively, this can be viewed as performing an inverse Fourier transform of the Hamiltonian $\widehat{\mathrm{H}}$ of Eq. (3) in the direction perpendicular to the surface and then restricting this operator with Dirichlet boundary conditions to a finite or semi-infinite z range. Dirichlet boundary conditions correspond to a straightforward truncation of the matrix between the layer block matrices, leading to

$$\widehat{\mathrm{H}}_{z<0}(\mathbf{k}_\parallel) = \begin{pmatrix} \widehat{\mathrm{H}}_{11}(\mathbf{k}_\parallel) & \widehat{\mathrm{H}}_{12}(\mathbf{k}_\parallel) & & \\ \widehat{\mathrm{H}}_{21}(\mathbf{k}_\parallel) & \widehat{\mathrm{H}}_{22}(\mathbf{k}_\parallel) & \widehat{\mathrm{H}}_{23}(\mathbf{k}_\parallel) & \\ & \widehat{\mathrm{H}}_{32}(\mathbf{k}_\parallel) & \widehat{\mathrm{H}}_{33}(\mathbf{k}_\parallel) & \\ & & & \ddots \end{pmatrix}, \tag{5}$$

where the interlayer and intralayer terms are given analogous to Eq. (3), but now only including vectors $\mathbf{R} : QL_i \to QL_j$, connecting unit cells from the ith and jth quintuple layers, in the sum,

$$\widehat{\mathrm{H}}_{ij}(\mathbf{k}_\parallel) = \sum_{\mathbf{R}:QL_i\to QL_j} \mathrm{H}_{\mathbf{R}}\, \mathrm{e}^{\mathrm{i}\mathbf{k}_\parallel\cdot\mathbf{R}}. \tag{6}$$

We note that, for materials in the Bi_2Se_3 family, which consist of weakly van der Waals bound quintuple layers, Dirichlet boundary conditions are a natural and very precise approximation. To keep our model as concise as possible, we neglect additional terms localized close to the boundary, such as a shift in the energies of the outermost orbitals.

The half-space Bloch functions are given *inside* the bulk of the crystal as

$$\Psi_{n,\mathbf{k}_\parallel}(\mathbf{r}) = \sum_{\nu\in I,\eta\in 1,..N_{QL}} \mathcal{C}^n_{\nu,\eta}(\mathbf{k}_\parallel) \sum_{\mathbf{R}\in\mathcal{L}} e^{i\mathbf{k}_\parallel\cdot\mathbf{r}} w_\nu(\mathbf{r}-\mathbf{R}), \tag{7}$$

where $\mathcal{C}^n(\mathbf{k}_\parallel)$ is the nth eigenvector of the square matrix $\widehat{\mathrm{H}}_{z<0}(\mathbf{k}_\parallel)$ with size $30\cdot N_{QL}$ and $w_\nu(\mathbf{r}-\mathbf{R})$ are the Wannier functions of the bulk material. For the spectroscopic experiments a description of the Bloch functions *outside* of a fictitious sample boundary is necessary. Calculating the Wannier functions of a film system or single quintuple layer from first-principles is computationally much more expensive than for the bulk. Thus the propagation of the Bloch functions into the vacuum is not calculated self-consistently in this paper. We assume the laterally averaged potential V at the boundary of the material to be

$$V(z) = \begin{cases} \Phi & \text{for} \quad z > z_b \\ 0 & \text{for} \quad z < z_b \end{cases}, \tag{8}$$

where Φ is the work function of the material and z_b denotes the position of the fictitious sample boundary. We take for the work functions the values $\Phi_{BS} = 5.6\,\mathrm{eV}$, $\Phi_{BTS} = 5.1\,\mathrm{eV}$, $\Phi_{BT} = 5.25\,\mathrm{eV}$ from Refs. [58,59] and from the Gundlach oscillations reported in [41,60–63]. We choose z_b such that the boundary lies 1.3 Å further out from the outermost atomic cores. In the following we rely on the expression of Bloch functions as

$$\Psi_{n,\mathbf{k}_\parallel}(\mathbf{r}) = e^{i\mathbf{k}_\parallel\cdot\mathbf{r}} u_{n,\mathbf{k}_\parallel}(\mathbf{r}), \tag{9}$$

where $u_{n,\mathbf{k}_\parallel}(\mathbf{r})$ has the periodicity of the lattice. Thus the function $u_{n,\mathbf{k}_\parallel}(\mathbf{r})$ restricted to the plane at the boundary of the sample is periodic, and can be developed into a two-dimensional Fourier series using the reciprocal surface lattice vectors G_Δ. For z *outside* the fictitious sample boundary

$$\Psi_{n,\mathbf{k}_\parallel}(\mathbf{r}) = \sum_{\mathbf{G}_\Delta\in\mathcal{RL}} c^\Delta_{n,\mathbf{k}_\parallel}\; d^\Delta_{n,\mathbf{k}_\parallel}(z)\; e^{i(\mathbf{k}_\parallel+\mathbf{G}_\Delta)\cdot\mathbf{r}_\parallel} \tag{10}$$

holds, with $d^\Delta_{n,\mathbf{k}_\parallel}(z) = \exp(-\kappa(\mathrm{n},\mathbf{k}_\parallel,\Delta)\,\mathrm{z})$ and the energy and momentum dependent decay constant given as

$$\kappa(n,\mathbf{k}_\parallel,\Delta) = \sqrt{\frac{2m}{\hbar^2}(\Phi - E_{n,\mathbf{k}_\parallel}) + (\mathbf{k}_\parallel+\mathbf{G}_\Delta)^2}. \tag{11}$$

We calculate the Fourier coefficients $c^\Delta_{n,\mathbf{k}_\parallel}$ by numerically approximating the integral

$$c^\Delta_{n,\mathbf{k}_\parallel} = \int_{\mathsf{UC}} e^{-i\mathbf{G}_\Delta\cdot\mathbf{r}} u_{n,\mathbf{k}_\parallel}(x,y,z_b)\,\mathrm{d}x\,\mathrm{d}y \tag{12}$$

over the two-dimensional surface unit cell UC with a finite sum over a 50×50 grid of $\mathbf{r}$ points in UC aligned with the surface lattice vectors. The decay constant $\kappa(n,\mathbf{k}_\parallel,\Delta)$ can be deduced from the solution of the Schrödinger equation of a free particle [64]. Upon examining Eq. (11) it becomes apparent that Bloch functions, which lie far below the Fermi energy E_F decay faster into the vacuum than those with higher energy. Also we see that the Bloch functions with $\mathbf{k}$ close to Γ propagate further into the vacuum. Furthermore, it is possible

to truncate the sum in Eq. (10) after the first three reciprocal lattice vectors, as the plane wave components with larger G_Δ decay rapidly outside the sample, such that their contribution is negligible.

C. Calculation of the tunneling current

The starting point is Bardeen's formula for the tunneling current [24,25]. The tunneling current I is sensitive to all electronic states with energy E between the Fermi energy E_F of the sample and $E_F + eU_B$, where U_B is the bias voltage applied to the tip sample junction,

$$I(U_B) = \text{const.} \cdot \text{sgn}(U_B) \cdot \sum_{E_\mu \in \mathcal{E}} \sum_{\nu \in \mathcal{I}} |M_{\mu\nu}|^2, \tag{13}$$

where $\mathcal{E} = [\min(E_F, E_F + eU_B), \max(E_F, E_F + eU_B)]$ and $\mathcal{I} = \{s,\ p_x,\ p_y,\ p_z\}$. For the differential conductance, only the states close to $E_F + eU_B$ are relevant,

$$\frac{\mathrm{d}I}{\mathrm{d}V}(U_B) = \text{const.} \cdot \sum_{E_\mu \approx E_F + eU_B} \sum_{\nu \in \mathcal{I}} |M_{\mu\nu}|^2. \tag{14}$$

The notation $E_\mu \approx E_F + eU_B$ indicates that the tunneling matrix elements are weighted by a Lorentzian and a semicircle function, incorporating finite energy resolution and modulation broadening. The tunneling matrix element between the sample wavefunction ψ_μ and the tip wavefunction χ_ν is given as an integral over a surface $\mathcal{S}$ separating tip and sample,

$$M_{\mu\nu} = -\frac{\hbar^2}{2m} \int_{\mathcal{S}} (\chi_\nu^* \nabla \psi_\mu - \psi_\mu \nabla \chi_\nu^*)\, \mathbf{d}\mathcal{S}. \tag{15}$$

Calculating this integral is computationally expensive and furthermore the precise tip wavefunctions χ_ν are not known [65]. Chen's derivative rule is an efficient approximation, relying on the expansion of the tip wavefunction χ_ν into spherical harmonics Y_{lm} centered at the position of the tip apex $\mathbf{r}_0$ [66]. This expansion is given by the sum

$$\chi_\nu(\mathbf{r}) = \sum_{lm} C_{\nu lm}\, k_l(\kappa_\nu r)\, Y_{lm}(\theta, \varphi) \tag{16}$$

where $r = |\mathbf{r} - \mathbf{r}_0|$, θ is the polar angle and φ the azimuthal angle. The function $k_l(\kappa_\nu r)$ is the lth Bessel function of the second kind, with κ_ν being the decay constant of the tip orbital into the vacuum. This expansion can also be done in terms of the real spherical harmonics with angular symmetries $\beta \in \{s, x, y, z, ...\}$, which are obtained as linear combinations of the complex-valued spherical harmonics. Introducing the notation $\widetilde{Y}_{\nu\beta} = k_\beta(\kappa_\nu r) Y_\beta(\theta, \varphi)$ the sum in Eq. (16) is equivalent to

$$\chi_\nu(\mathbf{r}) = \sum_\beta C_{\nu\beta}\, \widetilde{Y}_{\nu\beta}(\theta, \varphi). \tag{17}$$

Chen's derivative rule gives an approximation for evaluating the integral in Eq. (15) [25]. Based upon the expansion of the tip wavefunction $\chi_\nu(\mathbf{r})$ shown in Eq. (17) the tunneling matrix element can be approximated by

$$|M_{\mu\nu}|^2 = \frac{4\pi^2\hbar^4}{\kappa_\nu^2 m_e} \left| \sum_\beta C_{\nu\beta}\, \hat{\partial}_{\nu\beta}\, \psi_\mu(\mathbf{r}_0) \right|^2. \tag{18}$$

TABLE I. Correspondence between tip orbital character β and differential operator $\hat{\partial}_{\nu\beta}$ according to Chen's derivative rule. Prime coordinates correspond to the tip coordinate system.

Differential operators $\hat{\partial}_{\nu\beta}$ in the derivative rule				
β	s	x'	y'	z'
$\hat{\partial}_{\nu\beta}$	1	$\frac{1}{\kappa_\nu}\frac{\partial}{\partial x'}$	$\frac{1}{\kappa_\nu}\frac{\partial}{\partial y'}$	$\frac{1}{\kappa_\nu}\frac{\partial}{\partial z'}$

The differential operators $\hat{\partial}_{\nu\beta}$ act on the sample wavefunction ψ_μ and are evaluated at the position of the tip $\mathbf{r}_0$, they are given in Table I. As the Bloch functions $\Psi_{n,\mathbf{k}_\parallel}(\mathbf{r})$ are given as Fourier series in Eq. (10) the derivatives in x and y direction can be calculated by multiplying the Fourier coefficients $c^\Delta_{n,\mathbf{k}_\parallel}$ with the x and y components of $i\mathbf{k}_\parallel + \mathbf{G}_\Delta$. The z derivative is obtained by multiplying the plane wave components $e^{i(\mathbf{k}_\parallel + G_\Delta)\cdot\mathbf{r}}$ of $\Psi_{n,\mathbf{k}_\parallel}(\mathbf{r})$ with $-\kappa(n, \mathbf{k}_\parallel, \Delta)$.

For clarification, we note that the sum over the orbitals ν in Eq. (13) is a sum over magnitudes squared, whereas the sum in Eq. (18) over different spherical harmonics β contributing to one orbital ν takes the relative phases into account. For metal tips, it is sufficient to consider only the tunneling current through the s-type orbital [25]. In the case of CO-terminated tips, the p-type orbitals also contribute significantly to the tunneling current [67]. Orbitals with higher quantum number $n(\nu) \geqslant 2$ and corresponding differential operators with a higher order are not necessary for the tips used in the experiments presented here. The energy dependence of the constants κ_ν and $C_{\nu\beta}$ is not known, we use $k_\nu = 1\ \text{Å}^{-1}$ and constant $C_{\nu\beta}$ as given in Table II, similar to Refs. [67,68].

In order to correctly describe the tunneling through CO-terminated tips, the following considerations are necessary. The differential operators $\hat{\partial}_{\nu\beta}$ of Table I are given in the tip coordinate system, which might be tilted with respect to the sample coordinate system. With prime coordinates x', y', z' we denote the tip coordinate system, and with x, y, z we denote the sample coordinate system. Following the conventions of Ref. [65], these coordinate systems are related to each other by

$$(x'\ \ y'\ \ z')^{\mathrm{T}} = \text{Rot}(\phi, \psi, \theta)(x\ \ y\ \ z)^{\mathrm{T}}, \tag{19}$$

where ϕ, ψ, and θ are the Euler angles and the rotation matrix $\text{Rot}(\phi, \psi, \theta)$ is defined in the Supplemental Material [41]. There are two reasons, which make it necessary to consider the tilt of the CO-tip. First, CO-tips are rarely perfectly cylindrically symmetric. Second, because of lateral forces acting

TABLE II. Expansion coefficients for the s orbital of a metal tip and the s-, p_x-, and p_y orbital of a CO-tip in the tip coordinate system.

ν	$C_{\nu s}$	$C_{\nu x'}$	$C_{\nu y'}$	$C_{\nu z'}$
	Expansion coefficients for metal tip			
s	1	0	0	0
	Expansion coefficients for CO-tip			
s	1/2	0	0	0
p_x	0	$\sqrt{3/8}$	0	0
p_y	0	0	$\sqrt{3/8}$	0

on the apex atom the CO molecule will bend by a varying amount as a function of the lateral tip position. This effect becomes significant for the tip-sample separations of 3 Å − 4 Å, which were used for the experiments described in this article [69,70]. According to Ref. [65], the expansion coefficients in the tip coordinate system $C_{\nu i'}$ are related to those in the sample coordinate system by

$$\begin{pmatrix} C_{\nu x} \\ C_{\nu y} \\ C_{\nu z} \end{pmatrix} = \mathrm{Rot}(\phi, \psi, \theta)^{-1} \begin{pmatrix} C_{\nu x'} \\ C_{\nu y'} \\ C_{\nu z'} \end{pmatrix}. \tag{20}$$

The relaxation of the CO molecule upon approaching the sample can be calculated using the mechanistic probe-particle model (PPM) [71,72], which assumes that the interaction of the sample with the oxygen atom at the apex of the CO-tip is well described by a linear combination of Lennard-Jones potentials. In previous work we demonstrated that this model is well suited for describing atomic forces that act between the tip and the samples under investigation in this work [16]. We note that extensions of the PPM are able to simulate STM images with a relaxation of the probe particle; however, they do not consider the accompanying tilt of the tip orbitals [69,70].

IV. SCANNING TUNNELING SPECTROSCOPY AND HALF-SPACE BAND STRUCTURE

A. Bi_2Se_3

Unlike the other data and calculations presented in this article, Fig. 3 is concerned with a metal tip on the surface of Bi_2Se_3. This experiment is included to demonstrate that the methods used in this study are applicable to STS experiments with metal tips, which are commonly employed in preceding studies.

The calculated data in Figs. 3(a) and 3(b) were obtained on a 90 × 90 Monkhorst-Pack grid. The color coding of the half-space band structure in Fig. 3(c) indicates the base-10 logarithm of the square of the magnitude of the tunneling matrix element $M_{\mu,\nu}(\mathbf{k}_\parallel)$, which forms the basis of the calculation. Qualitatively, the $\mathrm{d}I/\mathrm{d}V$ spectrum in Fig. 3(a) closely resembles the spectrum obtained using the CO-terminated tip shown in Fig. 1(a). This similarity suggests that CO-terminated tips can in fact reliably reproduce $\mathrm{d}I/\mathrm{d}V$ results otherwise measured with metal tips.

Figure 3(b) shows the tunneling current, obtained from the calculation $I^{(theo.)}(E)$ in blue and from experiment $I^{(exp.)}(U_B)$ in orange. The theoretical current traces are calculated by integrating the calculated $\mathrm{d}I/\mathrm{d}V$ from the experimental Fermi energy $E_F^{(exp.)}$ to the energy E. These current traces are used to normalize the theoretical and experimental $\mathrm{d}I/\mathrm{d}V$ spectra. The method is described in detail in the Supplemental Material [41] and Ref. [73]. A nonzero slope of $I(U_B)$ for all bias voltage U_B indicates the closing of the band gap can be deduced from Fig. 3(b); however, the figure also demonstrates that the tunneling current is not adequate for an in-depth analysis of the electronic structure.

The theoretical and experimental $\mathrm{d}I/\mathrm{d}V$ signal is much more suitable for this purpose. Figure 3(a) shows the experimental spectrum of a metal tip on the surface of Bi_2Se_3 in orange and the calculated counterpart in blue. In experimental

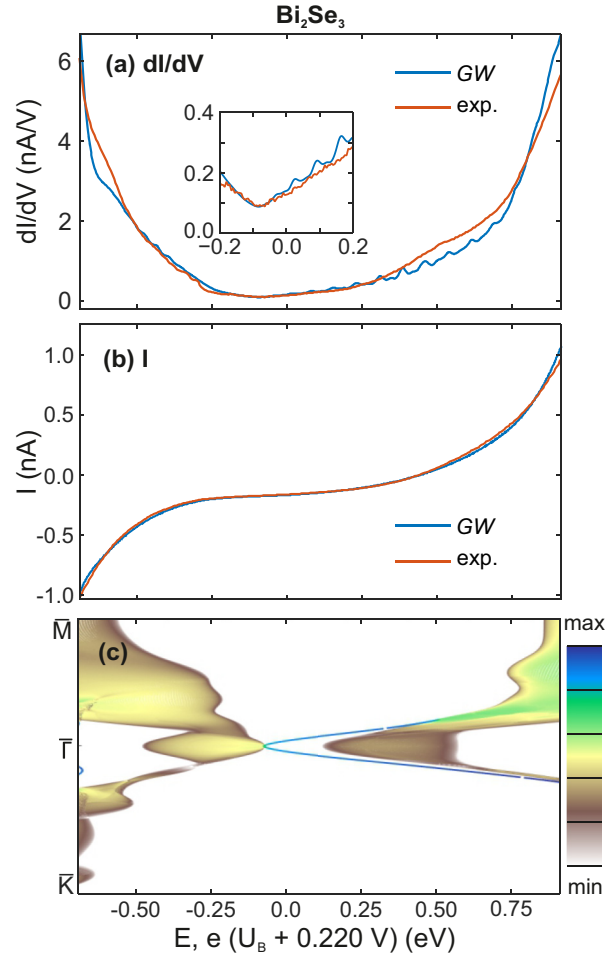

FIG. 3. (a) $\mathrm{d}I/\mathrm{d}V$ spectrum of a metal tip positioned above a selenium atom of the Bi_2Se_3 surface overlayed with the calculated spectrum. The inset shows the experimental and calculated $\mathrm{d}I/\mathrm{d}V$ for $-0.2\,\mathrm{V} < E < 0.2\,\mathrm{V}$ with adjusted y axis. (b) Experimental and calculated tunneling current. (c) Half-space band structure of Bi_2Se_3 color coded with $\log_{10}(|M_{\mu,\nu}(\mathbf{k}_\parallel)|^2)$. Each black line in the color bar of (b) indicates one order of magnitude.

practice, there is a shift of the Fermi level of the sample owing to native point defects [16]. Thus, to align the spectra we need to plot the energy E and the shifted bias voltage $U_B + \Delta E_F$ on the abscissa of Fig. 3. For the sample used during the measurements with a metal tip, shown in Fig. 3, we find $\Delta E_F = 0.22\,\mathrm{eV}$. This is comparable to the sample used for the measurements in Fig. 1(a), where this shift was equal to 0.24 eV.

Key features in the $\mathrm{d}I/\mathrm{d}V$ spectrum are the minimum in the differential conductance at $E_D = -0.08\,\mathrm{eV}$ with a linear increase of the differential conductance away from E_D. Comparison with the half-space band structure in Fig. 3(c) shows that this minimum in the $\mathrm{d}I/\mathrm{d}V$ spectrum corresponds to the energy of the Dirac point E_D.

Other important markers in the experimental $\mathrm{d}I/\mathrm{d}V$ spectrum are at $E = -0.7\,\mathrm{eV}$, $E = -0.25\,\mathrm{eV}$, and $E = 0.75\,\mathrm{eV}$, where the experimental $\mathrm{d}I/\mathrm{d}V$ signal significantly increases towards lower and higher energies, respectively. These features are reproduced by the theoretical $\mathrm{d}I/\mathrm{d}V$ spectrum in Fig. 3(a). Comparison to the half-space band structures in

Fig. 3(c) shows that both increases result from the bulk bands becoming less dispersive in the $\bar{\Gamma}$–$\bar{\mathrm{M}}$ direction. This flattening of the bands leads to an accumulation in energy and thus to an increased differential conductance.

However, we also note that there are discrepancies between the calculated and experimental spectra visible in Fig. 3(a). The major discrepancy is that the calculated $\mathrm{d}I/\mathrm{d}V$ spectrum is significantly lower than the experimental spectrum for $E = (0.5 \pm 0.11)$ eV. We first explain the behavior of the theoretical spectrum in this energy range and then focus on possible explanations for this discrepancy. In the theoretical calculation of Fig. 3(a), we see an approximately linear increase in the $\mathrm{d}I/\mathrm{d}V$ signal for $-0.09\,\mathrm{eV} < E < 0.75\,\mathrm{eV}$. In the $\bar{\Gamma}$–$\bar{\mathrm{K}}$ direction, the topological boundary mode remains distinct from the bulk modes up to $E = 0.75\,\mathrm{eV}$ and the tunneling matrix element associated with it retains a large magnitude. In the $\bar{\Gamma}$–$\bar{\mathrm{M}}$ direction, the topological boundary mode hybridizes with the bulk modes at $E = 0.49\,\mathrm{eV}$. Following the linear dispersion relation of the topological boundary mode, there is a set of bulk conduction bands associated with an increased tunneling probability, which appears in green in the color scale of Fig. 3(c). This is far beyond the conduction band minimum, which is located at $E = 0.15\,\mathrm{eV}$. Our calculation of the tunneling matrix elements associated with the conduction band edge shows a very small magnitude, such that states near the conduction band edge do not contribute to the calculated $\mathrm{d}I/\mathrm{d}V$ spectrum. The dispersion relation of the topological boundary mode in these two high-symmetry directions and the vanishing of the tunneling matrix element close to the CBM explain why the increase of the differential conductance follows the linear trend up to 0.75 eV. However, the maximum of the deviation at $E = (0.5 \pm 0.11)$ eV coincides with the presence of many flat conduction bands in the vicinity of Γ. A slight deviation in the calculation of the tunneling matrix element of these bands, for example owing to surface effects, might thus nonetheless explain the discrepancy between the experimental and calculated spectrum.

Another, rather minor discrepancy is the presence of small peaks in the calculated spectrum. These are numerical artifacts caused by the finite grid of **k** points used to approximate the Brillouin zone integral.

Finally, we want to discuss the topological boundary mode and its contribution to the $\mathrm{d}I/\mathrm{d}V$ signal in more detail. Both of the linear sections around E_D, clearly visible in the inset of in Fig. 3(a), are well reproduced by the calculation shown in blue. As discussed for the spectrum of a CO-terminated tip in Sec. II, we note that our calculation shows that the linear section for $E > E_D$ corresponds to tunneling into and out of the topological boundary mode. This interpretation agrees with previous reports [18]. For energies $-0.08\,\mathrm{eV} > E > -0.25\,\mathrm{eV}$ the topological surface state is strongly hybridized with parabolic bulk valence bands. In Fig. 4(a), the topological boundary mode appears as dark purple line crossing the bulk band gap with a linear dispersion. The valence band edge appears in light blue. The *GW* calculation indicates the Dirac point is located at the VBM. Below the VBM we see two darker features inside the valence band edge that continue along the linear dispersion of the topological boundary mode for $-0.08\,\mathrm{eV} > E - 0.25\,\mathrm{eV}$. These dark features correspond to the hybridization of the Dirac cone with the bulk bands.

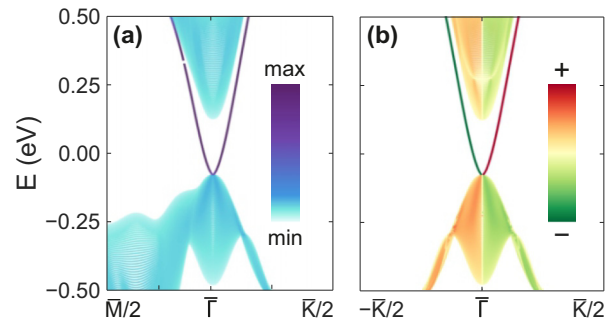

FIG. 4. (a) Half-space band structure of Bi_2Se_3 with color map representing the localization on the first QL. Following the linear dispersion of the upper Dirac cone there are darker lines inside the valence bands for $-0.08\,\mathrm{eV} > E > -0.25\,\mathrm{eV}$, which represent the strongly hybridized surface states. (b) Band structure from $-\bar{\mathrm{K}}/2$ to $\bar{\mathrm{K}}/2$ with color indicating expectation value on spin orthogonal to **k**. The spin polarization in the lower Dirac cone is minimal owing to the hybridization with the bulk bands.

The color map of Fig. 4(b) indicates the expectation value on the spin component orthogonal to **k**. In accordance with the previous observation the spin momentum polarization of the Dirac cone decreases rapidly upon hybridization with the bulk bands. The calculation of the theoretical $\mathrm{d}I/\mathrm{d}V$ spectrum shows that tunneling out of these hybridized bands reproduces the linear increase for $E < E_D$ in the $\mathrm{d}I/\mathrm{d}V$ spectrum. This is a modification of previous reports, where the lower linear section was attributed to a possible isolated lower half of the Dirac cone [18].

Summarizing these results, the dispersion of the topological boundary mode close to the Dirac point can be studied using STS and the observations are consistent with *GW* calculations of the band structure. Additionally, the $\mathrm{d}I/\mathrm{d}V$ spectrum reveals the energies where the dispersion of the bulk conduction and valence bands weakens, consistent with the calculated half-space band structure.

B. Bi_2Te_2Se

Figure 5(a) shows the experimental and calculated $\mathrm{d}I/\mathrm{d}V$ spectrum of a CO-terminated tip positioned on a Te atom on the surface of Bi_2Te_2Se. An atomic site with maximal distance to substitutional defects was chosen for this. The spectrum was recorded on a bias range from −0.4 V to 0.4 V. The corresponding half-space band structure is displayed in Fig. 5(b) with color coding analogous to that in Sec. IV A. The topological boundary mode of Bi_2Te_2Se appears in blue and green, which indicates the strong contribution of this mode to the differential conductance. The good agreement between theoretical and experimental characterization of the LDOS leads us to the following conclusions.

From the comparison in Fig. 5, a dopant induced shift of the Fermi level by $\Delta E_F = 0.01\,\mathrm{eV}$ can be determined, indicating a low level of bulk doping.

The energy of minimal differential conductance is −0.12 eV. Comparison to the half-space band structure conclusively shows that this does not correspond to the Dirac point. For energies below −0.12 eV tunneling into the bulk

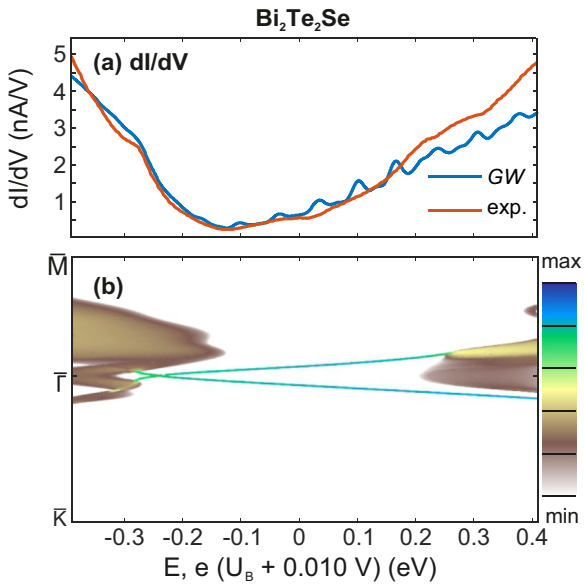

FIG. 5. (a) $\mathrm{d}I/\mathrm{d}V$ spectrum of a CO-tip positioned above a Te atom in the first atomic layer sites on the Bi_2Te_2Se surface. (b) half-space band structure of Bi_2Te_2Se around the bulk band gap color coded with $\log_{10}(|M_{\mu,\nu}(\mathbf{k}_\parallel)|^2)$. Each line in the color bar of (b) indicates one order of magnitude.

valence bands leads to an increase in the differential conductance. The position of the Dirac point is $E_D = -0.24\,\mathrm{eV}$, deep inside the bulk valence bands. At the Dirac point there is a plateau or shoulder like feature in the experimental and calculated $\mathrm{d}I/\mathrm{d}V$ spectrum. We attribute this to the flattening in the dispersion relation as the boundary mode hybridizes with the bulk modes. Also at this energy there are weakly dispersing surface resonances of the bulk valence bands visible in the $\bar{\Gamma}$–$\bar{\mathrm{K}}$ direction, which could also be a cause for observing this plateau-like feature. Previous measurements on Bi_2Te_2Se also documented this plateau-like feature in the $\mathrm{d}I/\mathrm{d}V$ spectrum [74].

As is the case for Bi_2Se_3, the tunneling matrix element of states at the bulk conduction band edge has a negligible contribution to the $\mathrm{d}I/\mathrm{d}V$ signal. The behavior of the topological boundary mode relative to the bulk conduction bands is similar to Bi_2Se_3 as well. In the $\bar{\Gamma}$–$\bar{\mathrm{K}}$ direction the boundary mode remains distinct from the bulk modes within the investigated energy range. Whereas in the $\bar{\Gamma}$–$\bar{\mathrm{M}}$ direction the boundary mode resonates strongly with the bulk modes, which can be seen as yellow region in bulk conduction bands, that continues along the linear dispersion of the boundary mode. As a result, for $-0.12\,\mathrm{eV} < E < 0.4\,\mathrm{eV}$ the experimental and calculated $\mathrm{d}I/\mathrm{d}V$ spectra follow a linear trend. Above $E = 0.2\,\mathrm{eV}$, there are some deviations from the linear trend in the experimental $\mathrm{d}I/\mathrm{d}V$ signal, which are not reproduced by the calculated spectrum. Possible reasons for this deviation include tunneling into bulk modes, which is not entirely described by our model, or the large density of substitutional defects in our Bi_2Te_2Se sample. Also, it was reported that a (trivial) two-dimensional electron gas (2DEG) can emerge at the surface of Bi_2Se_3, a compound very similar to Bi_2Te_2Se, owing to band bending at the interface to the vacuum surrounding the sample [75]. Energetically, this 2DEG occurs at the conduction band edge, which is where we observe the deviation of experiment and theory in Fig. 5(a), suggesting that it may explain the discrepancy. Based on the current analysis, it remains unclear which of these mechanisms is most relevant.

The energy range of Fig. 5 allows for a detailed investigation of the boundary mode and the Dirac cone; however, it is not large enough for observing the flattening in the dispersion of the bulk bands, as we discussed previously in Sec. IV A.

C. Bi_2Te_3

Figure 6(a) shows the $\mathrm{d}I/\mathrm{d}V$ spectrum of a CO-terminated tip positioned above a hollow site on the Bi_2Te_3 surface over a bias voltage range $-2\,\mathrm{V}$ to $2\,\mathrm{V}$. The experimental spectrum exhibits peaks in the differential conductance at $-1.2\,\mathrm{V}$, $-0.9\,\mathrm{V}$, $0.9\,\mathrm{V}$, and $1.75\,\mathrm{V}$. The orbital character of these peaks is discussed in Sec. VI A.

Figure 6(b) shows the *GW* band structure of Bi_2Te_3. The topological boundary mode appears in blue and green in the color coding of Fig. 6(b). The bulk valence bands appear in yellow and brown. In contrast, the bulk conduction bands are shown mostly in green, which corresponds to a larger magnitude of $M_{\mu,\nu}(\mathbf{k}_\parallel)$. This can be explained by a slower decay of the wave functions $\Psi_{n,\mathbf{k}}$ into the vacuum barrier, if $E_n(\mathbf{k})$ is larger. This relation is given quantitatively by Eq. (11) in Sec. III C, and thus can be understood on the level of effective noninteracting particles. As the DOS is approximately the same below and above E_F, this leads to a general trend in the $\mathrm{d}I/\mathrm{d}V$ spectrum of increasing differential conductance towards more positive energies in Fig. 6(a).

We associate the peaks in the $\mathrm{d}I/\mathrm{d}V$ spectrum with the accumulation of bulk bands and the flattening of their dispersion near the Brillouin zone boundary. For $E > 0$, there is a gap of approximately 0.5 eV between the lowest unoccupied bands

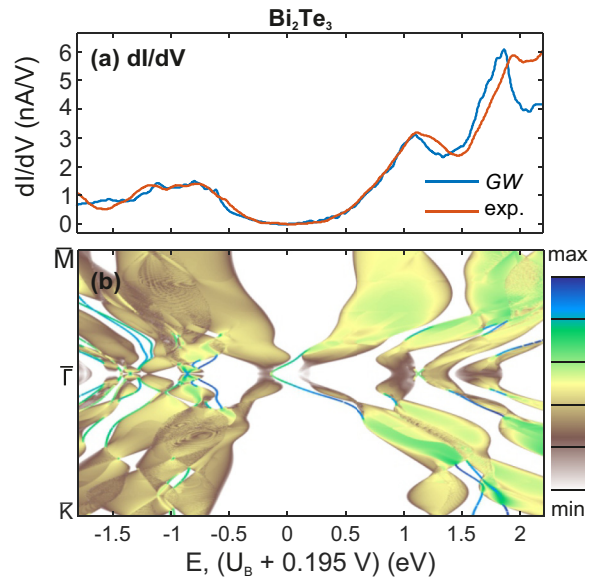

FIG. 6. (a) $\mathrm{d}I/\mathrm{d}V$ spectrum of a CO-tip positioned above a hollow site on the Bi_2Te_3 surface. (b) half-space band structure of Bi_2Te_3 color coded with $\log_{10}(|M_{\mu,\nu}(\mathbf{k}_\parallel)|^2)$. Each black line in the color bar of (b) indicates one order of magnitude.

and the next group of unoccupied bands as they approach the Brillouin zone boundary. This gap leads to the emergence of two distinct peaks at positive energies in the dI/dV spectrum shown in Fig. 6(a), separated by roughly the same energy gap. In contrast, for $E < 0$, the bulk bands exhibit significant overlap, resulting in less distinct peaks at negative energies. Additionally, we observe a Rashba and other surface states for $E < -0.5\,\mathrm{eV}$ in the vicinity of the Γ point as blue and green lines in Fig. 6(b). We assume that the contribution of these bands is small compared to the bulk bands. An experimental justification for this assumption can be derived from comparing the dI/dV signals across energy ranges where tunneling predominantly occurs into the topological boundary mode with respect to tunneling into bulk modes. The signal from tunneling into the bulk modes outweighs that from the topological boundary mode, despite the larger tunneling matrix element associated with the topological boundary mode. The magnitude of the tunneling matrix element for the nontopological surface states is of similar magnitude as the tunneling matrix element of the topological boundary mode. Therefore, it is reasonable to conclude that tunneling into the bulk modes is more significant in determining the overall dI/dV signal.

To the best of our knowledge, only very few experimental dI/dV measurements on this material class over such a large bias range have been published. There are experimental difficulties in obtaining spectra over this bias range. Because of the high bias voltage applied to the tip sample junction, large electrostatic forces act and a high current of up to 2 nA flows. Both effects increase the risk of a tip change or loss of the attached CO molecule. In our experiments, we increased the tip sample separation by 120 pm to limit the magnitude of the tunneling current and electrostatic forces. Furthermore, the likelihood of a spurious electronic tip state distorting the dI/dV spectrum increases with increasing energy range.

Despite this, studying spectra across extended energy ranges provides valuable insights. For instance, Ref. [15] examines energy level shifts caused by varying stoichiometry. Their theoretical density of states calculations span a similar energy range as shown in Fig. 6, whereas the experimental data of Ref. [15] covers only a much smaller range. Focusing only on a narrow energy scale is problematic since dI/dV spectra near the bulk band gap are generally featureless. Consequently, shifts in a single feature or changes in the vacuum barrier could be misinterpreted as shifts of the entire spectrum.

V. PROBING MANY-BODY CORRECTIONS

Our analysis in Sec. IV A shows that drastic changes in the half-space band structure of Bi_2Se_3 close to the Dirac point caused by the *GW* correction are in agreement with experimental observations. However, this does not provide the means to quantitatively show that *GW* aligns better with experiment than DFT. As an alternative approach to measurements that focus on the energy range near the Dirac point, we demonstrated in Sec. IV C, using Bi_2Te_3 as an example, that groups of bulk bands can be associated with peaks in the dI/dV spectrum appearing at higher energies. In the following section, we apply this method to characterize the effects of many-body corrections on the band structure of Bi_2Se_3,

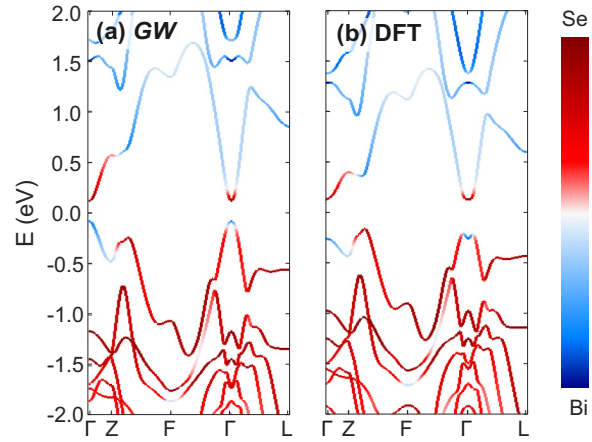

FIG. 7. (a) *GW* band structure and (b) DFT band structure of bulk Bi_2Se_3. DFT tends to underestimate trivial band gaps and overestimates nontrivial band gaps. The *GW* correction thus decreases the band gap around Γ but increases the separation between conduction and valence bands in the rest of the Brillouin zone. Furthermore, the *GW* correction removes the camelback shaped dispersion at the Γ point.

using the positions of these peaks as a quantitative measure of energy gaps.

First, we describe the main effects of the *GW* correction on the bulk band structure. In Fig. 7, both the bulk *GW* band structure (a) and the bulk DFT band structure (b) are plotted. The color code represents the orbital character of the Bloch functions. Blue indicates the corresponding Bloch function is primarily a linear combination of Wannier functions localized on Bi atoms and red indicates localization on the Se atoms. As expected, the valence bands primarily arise from the $3p$ orbitals of Se, and the conduction bands predominantly involve the $5p$ orbitals of Bi. In both band structures, the band inversion at the Γ point is evident. The *GW* correction tends to increase the magnitude of noninverted energy gaps while decreasing the magnitude of inverted gaps [22]. In topological insulators, this correction significantly alters the dispersion relation, as both inverted and noninverted energy gaps are present in the band structure.

The tendency of *GW* to increase the magnitude of noninverted energy gaps can be determined from the position of the bulk conduction bands at the L and F points. According to the DFT calculation the energy of the lowest unoccupied band at the L point is $E = -0.43\,\mathrm{eV}$ and of the highest occupied band is $E = 0.60\,\mathrm{eV}$, which leads to an energy gap of $\Delta E^{\mathrm{L}}_{\mathrm{DFT}} = 1.03\,\mathrm{eV}$. In the *GW* band structure, the energy of the lowest unoccupied band at the L point is $E = 0.85\,\mathrm{eV}$ and of the highest occupied band is $E = -0.55\,\mathrm{eV}$. Thus, the energy gap in the *GW* band structure is $\Delta E^{\mathrm{L}}_{GW} = 1.4\,\mathrm{eV}$, which is larger than $\Delta E^{\mathrm{L}}_{DFT} = 1.03\,\mathrm{eV}$ by about 36%. At the F point, we have $\Delta E^{\mathrm{F}}_{GW} = 2.4\,\mathrm{eV}$ and $\Delta E^{\mathrm{F}}_{\mathrm{DFT}} = 2.0\,\mathrm{eV}$. The influence of the *GW* correction on the value of the inverted band gap g at the Γ point is reversed. We find $g_{GW} = 0.21\,\mathrm{eV}$ and $g_{\mathrm{DFT}} = 0.24\,\mathrm{eV}$. Furthermore, the dispersion relation of the bulk conduction band at the Γ point is no longer camelback shaped in the *GW* band structure. The observations made for the bulk band structure also apply to the half-space band struc-

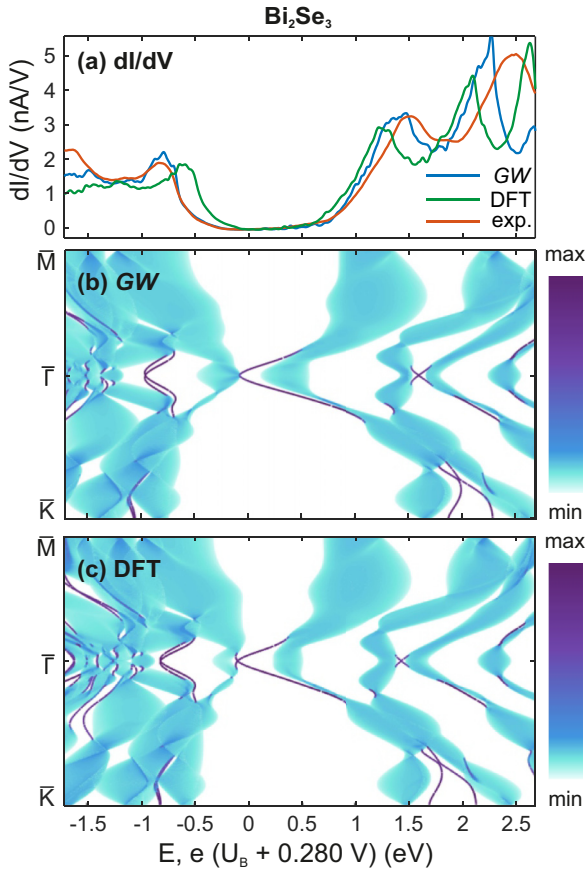

FIG. 8. (a) Comparison of experimentally obtained $\mathrm{d}I/\mathrm{d}V$ spectrum of a CO-tip positioned above a Se atom in the first atomic layer (orange) with the theoretical spectra calculated from the *GW* Hamiltonian (blue) and DFT Hamiltonian (red). (b) Half-space band structure of the *GW* Hamiltonian for Bi_2Se_3. (c) Half-space band structure of the DFT Hamiltonian for Bi_2Se_3.

tures shown in Figs. 8(b) and 8(c). Note that here the lowest unoccupied and the highest occupied bands are smeared out, but especially the lowest unoccupied bands are recognizable as distinct group of bands, separated from the rest of the band structure. The energy gap between the bulk modes, shown in light blue, at $\overline{\mathrm{K}}$ and $\overline{\mathrm{M}}$ is smaller in the DFT-band structure than in the *GW* band structure. More precisely, we have $\Delta E^{\overline{\mathrm{K}}}_{GW} = 2.4\,\mathrm{eV}$ and $\Delta E^{\overline{\mathrm{M}}}_{GW} = 1.41\,\mathrm{eV}$ in the *GW* band structure. In the DFT band structure, we find $\Delta E^{\overline{\mathrm{K}}}_{\mathrm{DFT}} = 2.03\,\mathrm{eV}$ and $\Delta E^{\overline{\mathrm{M}}}_{\mathrm{DFT}} = 1.07\,\mathrm{eV}$. Furthermore, the M-shaped dispersion relation at the Γ point in the case of the bulk DFT band structure is retained in the half-space DFT band structure. As a consequence of the inverted band curvature at Γ in the half-space DFT band structure, the Dirac point is buried beneath the valence band maximum.

The calculated and experimental $\mathrm{d}I/\mathrm{d}V$ spectra are plotted in Fig. 8(a). In the experimental spectrum, shown as orange curve, we observe local maxima in the differential conductance at $-0.8\,\mathrm{eV}$, $1.5\,\mathrm{eV}$, and $2.4\,\mathrm{eV}$. We denote by $\Delta E_{\mathrm{exp}} = 2.3\,\mathrm{eV}$ the difference between the peak at negative energies and the first peak at positive energies. We note that it is possible to distinguish Bi_2Se_3 from Bi_2Te_3 on the basis of the $\mathrm{d}I/\mathrm{d}V$ spectra in Figs. 6 and 8, as these three peaks are much farther apart in the case of Bi_2Se_3. The $\mathrm{d}I/\mathrm{d}V$ spectrum, which was calculated using the *GW* Hamiltonian, is plotted in blue in Fig. 8(a), whereas the DFT calculation is shown as the green line.

The *GW* calculation exhibits a closer alignment with the experimental data. *GW* reproduces the maxima in the experimental $\mathrm{d}I/\mathrm{d}V$ spectra at $E = -0.8\,\mathrm{eV}$ and $E = 1.5\,\mathrm{eV}$ with the correct position and amplitude. Furthermore, *GW* follows the development of the experimental $\mathrm{d}I/\mathrm{d}V$ signal around the bulk band gap closely. There is a sharp increase visible in the experimental $\mathrm{d}I/\mathrm{d}V$ spectrum at 0.75 eV, which is reproduced by the *GW* calculated $\mathrm{d}I/\mathrm{d}V$ spectrum. As established in Sec. IV A, this feature is the result of the flattening of the dispersion of the bulk conduction bands in the $\overline{\Gamma} - \overline{\mathrm{M}}$ direction. However, the *GW* calculation predicts the third peak in the spectrum to be at $E = 2.25\,\mathrm{eV}$, whereas this peak is located at $E = 2.5\,\mathrm{eV}$ in the experimental spectrum.

In contrast, the DFT calculation shows a noticeable shift in energy for all the observed peaks. Furthermore the trench in the DFT $\mathrm{d}I/\mathrm{d}V$ spectrum around the bulk band gap is narrower than in the experimental spectrum, reflecting the tendency of DFT to underestimate trivial gaps.

The difference of the two maxima around the bulk band gap in the experimental $\mathrm{d}I/\mathrm{d}V$ spectrum is $\Delta E_{\mathrm{exp}} = 2.3\,\mathrm{eV}$. We find that the numerical value of ΔE_{exp} lies in between the band gaps of the *GW* band structure at the $\overline{\mathrm{K}}$ and $\overline{\mathrm{M}}$ points, i.e.,

$$\Delta E^{\overline{\mathrm{K}}}_{GW} < \Delta E_{\mathrm{exp}} < \Delta E^{\overline{\mathrm{M}}}_{GW}. \tag{21}$$

In contrast, we find that both of the gaps in the DFT band structure, $\Delta E^{\overline{\mathrm{K}}}_{\mathrm{DFT}}$ and $\Delta E^{\overline{\mathrm{M}}}_{\mathrm{DFT}}$, are smaller than ΔE_{exp}. We conclude that DFT is able to qualitatively reproduce the shape of the experimental $\mathrm{d}I/\mathrm{d}V$ spectrum, but fails when it comes to predicting the quantitative energy gaps.

VI. ORBITAL COMPOSITION

Because of the very high spatial resolution of AFM and STM, it is possible to apply the previously presented results to determine the orbital contributions to the band structure. In the *spectral* method presented in Sec. VI A, we compare the $\mathrm{d}I/\mathrm{d}V$ signal as a function of energy with the tip being positioned above different inequivalent lattice sites. In Sec. VI B, the *spatial* method is introduced, where the $\mathrm{d}I/\mathrm{d}V$ signal is obtained as a function of the lateral tip position and we compare maps at different bias voltages U_B.

An experimental approach to achieve similar experimental results using ARPES is presented in Ref. [51]. In standing-wave excited hard x-ray photoemission spectroscopy (SW-HAXPES), atoms in the bulk crystal are excited using standing waves. Individual layers are excited with different intensity, owing to the distribution of nodes and antinodes of the standing wave pattern across the atomic layers. Because of the layered structure of Bi_2Se_3, the band structure can be studied element resolved using the technique described in Ref. [51]. However, unlike the experimental methods presented here, SW-HAXPES cannot be used to probe the unoccupied conduction bands.

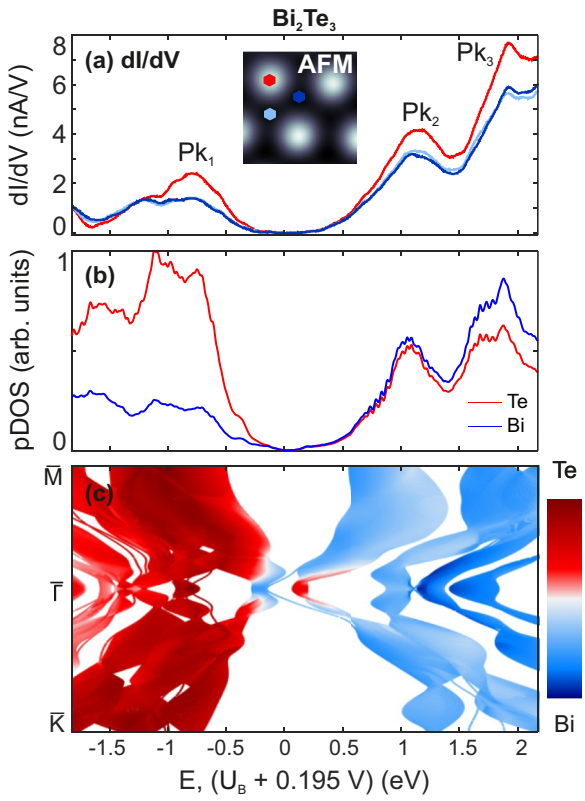

FIG. 9. (a) $\mathrm{d}I/\mathrm{d}V$ spectra of a CO-terminated tip on the three nonequivalent crystal sites on the Bi_2Te_3 surface. (b) Partial density of states corresponding to the Wannier functions localized on the Te and Bi positions in the first and second atomic layers. (c) Half-space band structure of Bi_2Te_3 with color representing orbital character of the energy bands.

A. Spectral method

Naturally, STS is not confined to studying only the occupied electron states, as electrons can tunnel from the tip into the sample and vice versa. Thus, the method we present here can be applied to characterize the orbital structure of the valence band relative to the conduction band. The experimental data underlying this analysis consist of $\mathrm{d}I/\mathrm{d}V$ spectra obtained on a Te site (red) and the two nonequivalent off-sites O1 and O2 (shades of blue), as shown in Fig. 9(a). The inset shows the frequency shift channel of an AFM measurement, where the Te atoms are imaged as bright spots. The lateral positions at which the spectra have been measured are indicated with the corresponding colors.

The characteristic peaks, marked by Pk_1, Pk_2, and Pk_3, as discussed in Secs. IV C and V, can be attributed to groups of weakly dispersing bulk bands. Table III lists the maximum differential conductance at these peaks for each crystal site. Furthermore, for a direct comparison the ratio

$$\mathcal{R} = \frac{\mathrm{d}I/\mathrm{d}V\,(\mathrm{O1},\mathrm{O2})}{\mathrm{d}I/\mathrm{d}V\,(\mathrm{Te})} \tag{22}$$

is given. The range of values for Pk_2 and Pk_3 results from the slight difference in the $\mathrm{d}I/\mathrm{d}V$ signal above O1 and O2.

For the first peak Pk_1 at negative energy, we see a drastic reduction of the peak amplitude giving $\mathcal{R} = 59\%$, when moving the tip from the Te site to the off-site. This can be explained by the fact that the valence bands are formed primarily by Te orbitals. This can be seen from the partial DOS shown in Fig. 9(b), which indicates that the partial DOS associated with the Te atoms is much larger than the partial DOS associated with Bi for negative energies $E < -0.5\,\mathrm{eV}$.

However, also for the peaks at positive energies we observe a reduction in the differential conductance when moving away from the Te site. Because of the exponential localization of the Wannier functions, the main contribution to the $\mathrm{d}I/\mathrm{d}V$ signal comes from the components of the Bloch functions localized on the Te atoms in the first atomic layer. In contrast to the valence bands, the conduction bands localize more evenly on the Te and Bi sites, as can be seen from the partial DOS shown in Fig. 9(b). Thus, for positive energies, increased tunneling into Bi orbitals is outweighed by a decreased tunneling into Te orbitals, leading to a small reduction of Pk_2 and Pk_3. However, the ratio $\mathcal{R}$ is only 73–80% for the peaks Pk_2 and Pk_3 at positive energies.

We base our analysis on the ratio $\mathcal{R}$ instead of the difference $\mathsf{dI/dV(O1, O2)} - \mathsf{dI/dV(Te)}$, which would be a physical quantity, but cannot be compared across different energies, owing to exponential damping in the vacuum barrier. Correcting for the vacuum tunneling barrier is not straightforward [76,77].

The observations here are what we expect from the band structure plotted in Fig. 9(c). Bands that are localized mostly on the Te orbitals appear red and the Bi bands are plotted in blue. A dark tone indicates strong localization, a lighter shade indicates weaker localization. The valence bands appear in a dark red, whereas the conduction bands are plotted in light blue color, confirming that the conduction bands localize more evenly on the Te and Bi than the valence bands. The band inversion at Γ is clearly visible in the half-space band structure.

TABLE III. Differential conductance at the peaks of the spectra shown in Fig. 9(a) and the ratio $\mathcal{R}$ of the peak height at the hollow sites O1 and O2 relative to the Te atomic site.

	Pk_1	Pk_2	Pk_3
Te	2.39 nA/V	4.14 nA/V	7.71 nA/V
O1	1.41 nA/V	3.32 nA/V	5.64 nA/V
O2	1.41 nA/V	3.17 nA/V	5.90 nA/V
$\mathcal{R}$	59%	(77–80)%	(73–77)%

B. Spatial method

In Ref. [78], it was demonstrated that the electronic structure of GaAs results in bias-dependent imaging in constant-current STM, where either the Ga atoms or the As atoms are selectively visible. For negative bias voltages, tunneling out of the occupied states makes the As appear bright, whereas for positive voltages the Ga atoms are mapped as topographic protrusions. Figure 10 shows the half-space band structure of Bi_2Se_3 with the color indicating the projection of the Bloch functions onto the Wannier functions localized on the Bi and Se atomic sites, respectively. The half-space band structure indicates that the valence bands are primarily formed

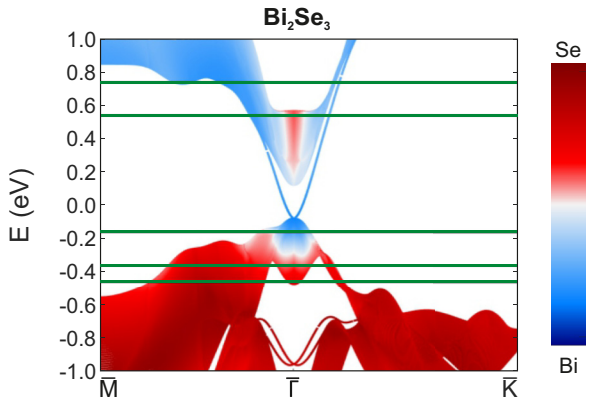

FIG. 10. Orbital weighted half-space band structure of Bi_2Se_3. The occupied bands are a linear combination of Wannier functions localized on the selenium atomic positions, whereas the unoccupied bands are localized mostly on the bismuth atoms. The band inversion at the $\bar{\Gamma}$ point can be observed as the reverse ordering of the colors. Green lines indicate energies of the dI/dV maps.

by orbitals of Se, whereas the conduction bands consist mostly of Bi orbitals. In this respect, Bi_2Se_3 has a lot in common with other binary compound semiconductors. However, the band inversion at Γ, giving rise to the topological boundary mode, can be discerned clearly.

In this article, we use a refinement of the method presented in Ref. [78]. We measure the differential conductance dI/dV instead of the total conductance. This allows us to probe the electronic state at a certain energy E instead of probing all states between E and the Fermi energy E_F. This is especially important, as in Bi_2Se_3 the lower conduction bands are occupied. As a result, the tunneling current is formed through a complex interplay of contributions from states strongly localized on Bi atoms and those strongly localized on Se atoms. Green horizontal lines in Fig. 10 represent the energies at which dI/dV maps were measured. The experimental dI/dV images at these energies are shown in Figs. 11(a)–11(e). The calculated dI/dV maps at the corresponding energies are shown in Figs. 11(a*)–11(e*). In the experimental images, the lateral position of the Se atoms is indicated by a red dot, which was determined by the maximum repulsive force in the simultaneously recorded frequency shift image [16,41]. Additionally, in the calculated images, the lateral position of the Bi atoms is plotted as a blue dot. Note that the data was measured using the same tip and sample as for the spectrum shown in Fig. 1(a). We use the dI/dV spectrum obtained in the same height as the dI/dV maps to represent the data of Fig. 11 in nA/V, using the method described in the Supplemental Material [41]. However, we need to account for a 30 pm vertical drift during the measurement of the dI/dV maps.

Taking the relaxation of the CO molecule into account is necessary to achieve satisfactory agreement between experiment and theory in Fig. 11. This relaxation was calculated using the PPM [71,72]. The bending of the CO molecule leads to a transformation of the derivatives for describing the tunneling through p-type orbitals, as described in Sec. III C, and also to a deflection of the position of the oxygen atom, which transmits most of the tunneling current. A more detailed discussion can be found in the Supplemental Material [41].

For energies within the bulk valence band, i.e., Figs. 11(a), 11(b), 11(a*), and 11(b*), we observe the Se atoms as bright features connected by fainter lines. We note good agreement between experiment and theory. The Se atoms do not appear spherical, but rather as slightly irregular hexagons. This deformation, as well as the lines, can be traced back to the bending of the CO molecule attached to the tip [41]. In the calculated image, the off sites at which the Bi atoms are located are brighter than the empty off sites, which is not the case in the experimental data shown in Figs. 11(a)

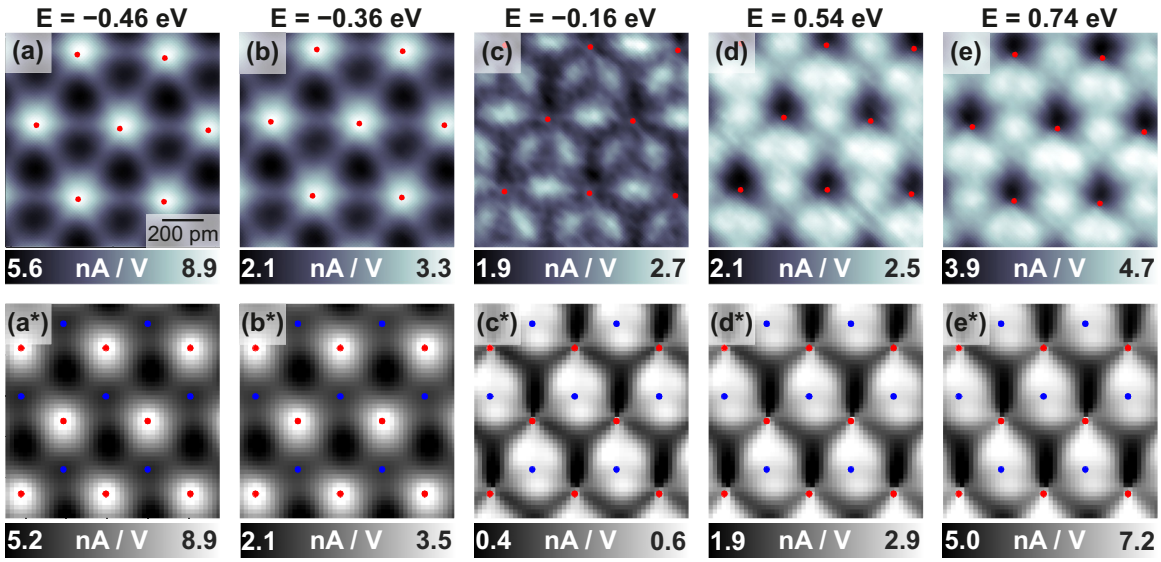

FIG. 11. (a)–(e) Experimentally obtained dI/dV maps for varying bias voltage between tip and sample. (a*)–(e*) Calculated dI/dV maps of the Bi_2Se_3 at various energies distributed throughout the valence and conduction bands. Red dots indicate the lateral position of the Se atoms and in the theoretical images blue dots indicate the lateral position of Bi atoms. Lateral drift of the Se atoms between the individual measurements is present in the experimental data.

and 11(b). The half-space band structure of Bi_2Se_3 indicates strong localization of the Bloch bands on the Se atoms, which is in agreement with the experimental observation. Our interpretation for negative energies agrees with previous experimental observations on Bi_2Se_3 and accompanying calculations of the LDOS from first-principles [10].

In Figs. 11(c) and 11(c*), close to the VBM, we observe lines or elongated maxima between the Se atoms in both the experimental and calculated images. In contrast to Panels (a), (a*), (b) and (b*), we no longer observe the Se atoms as bright features. Furthermore, in the theoretical data of Fig. 11(c*), the empty off sites appear as dark Y-shaped feature. Centered on the Bi sites there is a ⅄-shaped region, with three Se atoms at the ends. This ⅄ shape is dimmer than the elongated maxima along the direct connecting lines between each pair of Se atoms. In the experimental data shown in Fig. 11(c), we see similar tendencies. However, the ⅄-shaped feature is only slightly brighter than the Y centered on the other off site. The elongated maxima between the pairs of Se atoms are much brighter than both the Y and ⅄ shape. An energy dependent variation of the mix of tip orbitals might explain this variation in the brightness. The half-space band structure in Fig. 10 indicates that an energy of $E = -0.16\,\mathrm{eV}$ corresponds to the valence band edge, where the bands are inverted, explaining the absence of electronic states localized on the Se atoms that contribute to the $\mathrm{d}I/\mathrm{d}V$ signal. As the Bi atoms are located in the second atomic layer, the Bloch states localized on the Bi are not directly observed as bright features.

For positive energies, i.e., Panels (d), (d*), (e), and (e*) we observe bright features on the upwards facing off sites, corresponding to the Bi sites. These bright features consist again of elongated features with a high strength of the $\mathrm{d}I/\mathrm{d}V$ signal connecting pairs of Se atoms and dimmer ⅄-shaped regions centered on the upwards facing off sites. On the empty off-site we observe dark Y-shaped features connecting the Se atoms. In the experimental images, the Se atoms appear as dark images, whereas in the theoretical images we see sharp, bright lines at the Se atoms. This tendency might be explained by the fact that we do not consider the convolution of tip and sample wavefunction, as shown in Eq. (15), but instead applied Chen's derivative rule. The calculated images might not be as smooth as the experimental images, as a result of not considering this convolution. From the half-space band structure in Fig. 10 we might have expected the Se atoms to appear bright in Fig. 11(d) owing to the band inversion. However, the band inversion at the conduction band edge appears only in light red. Thus, the color map of Fig. 10 indicates only a weak localization on the Se atoms. Furthermore, the conclusion in Sec. IV A demonstrated that the states at conduction band edge close to $\bar{\Gamma}$ have a negligible contribution to the $\mathrm{d}I/\mathrm{d}V$ signal as opposed to the states farther away from $\bar{\Gamma}$ in this energy region. The states at the conduction band edge farther away from $\bar{\Gamma}$ that contribute strongly to the $\mathrm{d}I/\mathrm{d}V$ signal, are, however, again localized predominantly on the Bi atoms, explaining why we do not observe an increased $\mathrm{d}I/\mathrm{d}V$ signal above the Se atoms because the band inversion at the conduction band edge.

In the model presented here, there are possible improvements. We note that in all calculated images of Fig. 11, we assumed that the linear combination of wavefunctions at the tip does not depend on the energy E. Making this linear combination energy dependent might increase the agreement between experiment and theory, but introduces additional parameters. Another possible improvement is including bias and current dependent tip-sample forces in the PPM calculation. This includes electrostatic forces or current-induced electrostatic forces [79], which might add to the deflection of the CO molecule.

VII. OUTLOOK

Incorporating defects into the tight-binding model, as outlined in Ref. [80], allows for the study of point defect signatures using the presented method. Comparing theoretical and experimental $\mathrm{d}I/\mathrm{d}V$ spectra enables precise calibration of the energy scale, while the real-space sensitivity allows for selectively probing defect states on the atomic scale [21]. Furthermore, it is conceivable to adapt our calculations further and study the evolution of the band structure in moiré patterned samples [81] or the changes induced by external magnetic fields [82–84]. Future applications of the methods presented here include observing local topological phase transitions, possibly induced by strain [85] or by substitutional atoms [35]. From a fundamental and theoretical perspective the robustness of the boundary mode against crystal defects and changes in geometry of the crystal boundary has come into focus [86,87]. The derivation of the topological invariants by means of Bloch theory relies heavily on translational invariance. Consequently, it is not clear how the topological classification of materials extends to disordered materials. We believe that the experimental results presented here establish that combined scanning tunneling microscopy (STM) and atomic force microscopy (AFM) is an important tool for research in this area, as it is able to simultaneously characterize samples structurally and electronically from the atomic scale upward.

ACKNOWLEDGMENTS

We are thankful for very interesting discussions with Christoph Friedrich and his support with the use of the code SPEX. We are grateful to Stefan Blügel for establishing the contact between experiment and theory. We thank Marco Weiss for implementing a LabView program for automated measurement of $\mathrm{d}I/\mathrm{d}V$ maps. For the first-principles calculations, the computational resources were provided by the Dutch national e-infrastructure with the support of the SURF Cooperative under Grants No. EINF-5380 and No. EINF-10348. We acknowledge the financial support of the Deutsche Forschungsgemeinschaft through Project No. 314695032-SFB1277 (Subprojects No. A01, No. A08, and No. B02). We are thankful to Jay Weymouth and Fabian Stilp for careful proofreading.

[1] D. J. Thouless, M. Kohmoto, M. P. Nightingale, and M. den Nijs, Quantized Hall conductance in a two-dimensional periodic potential, Phys. Rev. Lett. **49**, 405 (1982).

[2] C. L. Kane and E. J. Mele, Quantum spin Hall effect in graphene, Phys. Rev. Lett. **95**, 226801 (2005).

[3] C. L. Kane and E. J. Mele, $\mathbb{Z}_2$ topological order and the quantum spin Hall effect, Phys. Rev. Lett. **95**, 146802 (2005).

[4] L. Fu, C. L. Kane, and E. J. Mele, Topological insulators in three dimensions, Phys. Rev. Lett. **98**, 106803 (2007).

[5] B. Lv, T. Qian, and H. Ding, Angle-resolved photoemission spectroscopy and its application to topological materials, Nat. Rev. Phys. **1**, 609 (2019).

[6] T. Knispel, W. Jolie, N. Borgwardt, J. Lux, Z. Wang, Y. Ando, A. Rosch, T. Michely, and M. Grüninger, Charge puddles in the bulk and on the surface of the topological insulator $BiSbTeSe_2$ studied by scanning tunneling microscopy and optical spectroscopy, Phys. Rev. B **96**, 195135 (2017).

[7] T. Mayer, H. Werner, F. Schmid, R. Diaz-Pardo, J. Fujii, I. Vobornik, C. H. Back, M. Kronseder, and D. Bougeard, Transport properties of band engineered $p-n$ heterostructures of epitaxial $Bi_2Se_3/(Bi_{1-x}Sb_x)_2(Te_{1-y}Se_y)_3$ topological insulators, Phys. Rev. Mater. **5**, 014202 (2021).

[8] L. Pietanesi, M. Marganska, T. Mayer, M. Barth, L. Chen, J. Zou, A. Weindl, A. Liebig, R. Díaz-Pardo, D. Suri, F. Schmid, F. J. Giessibl, K. Richter, Y. Tserkovnyak, M. Kronseder, and C. H. Back, Tracing Dirac points of topological surface states by ferromagnetic resonance, Phys. Rev. B **109**, 064424 (2024).

[9] F. J. Giessibl, The qPlus sensor, a powerful core for the atomic force microscope, Rev. Sci. Instrum. **90**, 011101 (2019).

[10] S. Urazhdin, D. Bilc, S. D. Mahanti, S. H. Tessmer, T. Kyratsi, and M. G. Kanatzidis, Surface effects in layered semiconductors Bi_2Se_3 and Bi_2Te_3, Phys. Rev. B **69**, 085313 (2004).

[11] Y. S. Hor, A. Richardella, P. Roushan, Y. Xia, J. G. Checkelsky, A. Yazdani, M. Z. Hasan, N. P. Ong, and R. J. Cava, p-type Bi_2Se_3 for topological insulator and low-temperature thermoelectric applications, Phys. Rev. B **79**, 195208 (2009).

[12] M. Romanowich, M.-S. Lee, D.-Y. Chung, S. D. Mahanti, M. G. Kanatzidis, and S. H. Tessmer, Interplay of topological surface and bulk electronic states in Bi_2Se_3, Phys. Rev. B **87**, 085310 (2013).

[13] M. Jurczyszyn, M. Sikora, M. Chrobak, and L. Jurczyszyn, Studies of surface states in Bi_2Se_3 induced by the BiSe substitution in the crystal subsurface structure, Appl. Surf. Sci. **528**, 146978 (2020).

[14] M. Teague, H. Chu, F.-X. Xiu, L. He, K.-L. Wang, and N.-C. Yeh, Observation of Fermi-energy dependent unitary impurity resonances in a strong topological insulator Bi_2Se_3 with scanning tunneling spectroscopy, Solid State Commun. **152**, 747 (2012).

[15] A.-M. Netsou, D. A. Muzychenko, H. Dausy, T. Chen, F. Song, K. Schouteden, M. J. Van Bael, and C. Van Haesendonck, Identifying native point defects in the topological insulator Bi_2Te_3, ACS Nano **14**, 13172 (2020).

[16] A. Liebig, C. Setescak, A. Weindl, and F. J. Giessibl, Structural characterization of defects in the topological insulator Bi_2Se_3 at the picometer scale, J. Phys. Chem. C **126**, 21716 (2022).

[17] Z. Alpichshev, J. G. Analytis, J.-H. Chu, I. R. Fisher, Y. L. Chen, Z. X. Shen, A. Fang, and A. Kapitulnik, STM imaging of electronic waves on the surface of Bi_2Te_3: Topologically protected surface states and hexagonal warping effects, Phys. Rev. Lett. **104**, 016401 (2010).

[18] A. Y. Dmitriev, N. I. Fedotov, V. F. Nasretdinova, and S. V. Zaitsev-Zotov, Effect of surface defects and few-atomic steps on the local density of states of the atomically-clean surface of Bi_2Se_3 topological insulator, JETP Lett. **100**, 398 (2014).

[19] N. I. Fedotov and S. V. Zaitsev-Zotov, Experimental search for one-dimensional edge states at surface steps of the topological insulator Bi_2Se_3: Distinguishing between effects and artifacts, Phys. Rev. B **95**, 155403 (2017).

[20] J. R. Moes, J. F. Vliem, P. M. M. C. de Melo, T. C. Wigmans, A. R. Botello-Méndez, R. G. Mendes, E. F. van Brenk, I. Swart, L. M. Licerán, H. T. C. Stoof *et al.*, Characterization of the edge states in colloidal Bi_2Se_3 platelets, Nano Lett. **24**, 5110 (2024).

[21] R. Queiroz, R. Ilan, Z. Song, B. A. Bernevig, and A. Stern, Ring states in topological materials, arXiv:2406.03529.

[22] I. Aguilera, C. Friedrich, and S. Blügel, Many-body corrected tight-binding Hamiltonians for an accurate quasiparticle description of topological insulators of the Bi_2Se_3 family, Phys. Rev. B **100**, 155147 (2019).

[23] N. Marzari, A. A. Mostofi, J. R. Yates, I. Souza, and D. Vanderbilt, Maximally localized Wannier functions: Theory and applications, Rev. Mod. Phys. **84**, 1419 (2012).

[24] J. Bardeen, Tunnelling from a many-particle point of view, Phys. Rev. Lett. **6**, 57 (1961).

[25] C. J. Chen, Tunneling matrix elements in three-dimensional space: The derivative rule and the sum rule, Phys. Rev. B **42**, 8841 (1990).

[26] T. Hofmann, Hochauflösende Rasterkraftmikroskopie auf Graphen und Kohlenmonoxid, Ph.D. thesis, Universität Regensburg, 2014.

[27] A. Liebig, A. Peronio, D. Meuer, A. J. Weymouth, and F. J. Giessibl, High-precision atomic force microscopy with atomically-characterized tips, New J. Phys. **22**, 063040 (2020).

[28] L. Bartels, G. Meyer, and K.-H. Rieder, Controlled vertical manipulation of single CO molecules with the scanning tunneling microscope: A route to chemical contrast, Appl. Phys. Lett. **71**, 213 (1997).

[29] H. Zhang, C.-X. Liu, X.-L. Qi, Z. Fang and S.C. Zhang *et al.*, Topological insulators in Bi_2Se_3, Bi_2Te_3 and Sb_2Te_3 with a single Dirac cone on the surface., Nat. Phys. **5**, 438 (2009).

[30] N. W. Ashcroft and N. D. Mermin, *Solid State Physics* (Cengage Learning, New York, 1976).

[31] B. Leung and E. Prodan, Effect of strong disorder in a three-dimensional topological insulator: Phase diagram and maps of the $\mathbb{Z}_2$ invariant, Phys. Rev. B **85**, 205136 (2012).

[32] C. M. Acosta, M. P. Lima, A. J. R. da Silva, A. Fazzio, and C. H. Lewenkopf, Tight-binding model for the band dispersion in rhombohedral topological insulators over the whole Brillouin zone, Phys. Rev. B **98**, 035106 (2018).

[33] I. A. Nechaev, R. C. Hatch, M. Bianchi, D. Guan, C. Friedrich, I. Aguilera, J. L. Mi, B. B. Iversen, S. Blügel, P. Hofmann, and E. V. Chulkov, Evidence for a direct band gap in the topological insulator Bi_2Se_3 from theory and experiment, Phys. Rev. B **87**, 121111(R) (2013).

[34] M. Orlita, B. A. Piot, G. Martinez, N. K. S. Kumar, C. Faugeras, M. Potemski, C. Michel, E. M. Hankiewicz, T. Brauner, i. c. v. Drašar, S. Schreyeck, S. Grauer, K. Brunner, C. Gould, C. Brüne, and L. W. Molenkamp, Magneto-optics of massive Dirac fermions in bulk Bi_2Se_3, Phys. Rev. Lett. **114**, 186401 (2015).

[35] J. Sánchez-Barriga, I. Aguilera, L. V. Yashina, D. Y. Tsukanova, F. Freyse, A. N. Chaika, C. Callaert, A. M. Abakumov, J. Hadermann, A. Varykhalov, E. D. L. Rienks, G. Bihlmayer, S. Blügel, and O. Rader, Anomalous behavior of the electronic structure of $(Bi_{1-x}In_x)_2Se_3$ across the quantum phase transition from topological to trivial insulator, Phys. Rev. B **98**, 235110 (2018).

[36] K. Kobayashi, Electron transmission through atomic steps of Bi_2Se_3 and Bi_2Te_3 surfaces, Phys. Rev. B **84**, 205424 (2011).

[37] M. K. Fuccillo, S. Jia, M. E. Charles, and R. J. Cava, Thermoelectric properties of Bi_2Te_2Se compensated by native defects and Sn doping, J. Electron. Mater. **42**, 1246 (2013).

[38] M. Neupane, S.-Y. Xu, L. A. Wray, A. Petersen, R. Shankar, N. Alidoust, C. Liu, A. Fedorov, H. Ji, J. M. Allred, Y. S. Hor, T.-R. Chang, H.-T. Jeng, H. Lin, A. Bansil, R. J. Cava, and M. Z. Hasan, Topological surface states and Dirac point tuning in ternary topological insulators, Phys. Rev. B **85**, 235406 (2012).

[39] H. Bruus and K. Flensberg, *Many-Body Quantum Theory in Condensed Matter Physics: An Introduction*, Oxford Graduate Texts (Oxford University Press, Oxford, 2004).

[40] Y. Zhang, K. He, C.-Z. Chang, C.-L. Song, L.-L. Wang, X. Chen, J.-F. Jia, Z. Fang, X. Dai, W.-Y. Shan *et al.*, Crossover of the three-dimensional topological insulator Bi_2Se_3 to the two-dimensional limit, Nat. Phys. **6**, 584 (2010).

[41] See Supplemental Material at http://link.aps.org/supplemental/10.1103/PhysRevB.111.165305 for a description of the experimental methods, sample preparation, our calibration methods for the dI/dV spectra, additional calculations, a discussion of tip relaxation and the measurements that were used to determine the work functions.

[42] Z.-H. Zhu, G. Levy, B. Ludbrook, C. N. Veenstra, J. A. Rosen, R. Comin, D. Wong, P. Dosanjh, A. Ubaldini, P. Syers, N. P. Butch, J. Paglione, I. S. Elfimov, and A. Damascelli, Rashba spin-splitting control at the surface of the topological insulator Bi_2Se_3, Phys. Rev. Lett. **107**, 186405 (2011).

[43] E. Grasser, Native point defects and standing waves - scanning probe microscopy of the topological insulator Bi_2Te_3, Bachelor thesis, Universität Regensburg, 2021.

[44] N. Fedotov, A. Maizlakh, V. Pavlovskiy, G. Rybalchenko, and S. Zaitsev-Zotov, Scanning tunneling microscopy of Bi_2Te_3 films prepared by pulsed laser deposition: From nanocrystalline structures to van der Waals epitaxy, Surf. Interfaces **31**, 102015 (2022).

[45] The MathWorks Inc., MATLAB version: 9.11.0.1769968 (R2021b) (2021).

[46] www.flapw.de.

[47] C. Friedrich, S. Blügel, and A. Schindlmayr, Efficient implementation of the GW approximation within the all-electron FLAPW method, Phys. Rev. B **81**, 125102 (2010).

[48] I. Aguilera, C. Friedrich, and S. Blügel, Spin-orbit coupling in quasiparticle studies of topological insulators, Phys. Rev. B **88**, 165136 (2013).

[49] I. Aguilera, C. Friedrich, G. Bihlmayer, and S. Blügel, *GW* study of topological insulators Bi_2Se_3, Bi_2Te_3, and Sb_2Te_3: Beyond the perturbative one-shot approach, Phys. Rev. B **88**, 045206 (2013).

[50] M. Michiardi, I. Aguilera, M. Bianchi, V. E. de Carvalho, L. O. Ladeira, N. G. Teixeira, E. A. Soares, C. Friedrich, S. Blügel, and P. Hofmann, Bulk band structure of Bi_2Te_3, Phys. Rev. B **90**, 075105 (2014).

[51] C.-T. Kuo, S.-C. Lin, J.-P. Rueff, Z. Chen, I. Aguilera, G. Bihlmayer, L. Plucinski, I. L. Graff, G. Conti, I. A. Vartanyants, C. M. Schneider, and C. S. Fadley, Orbital contributions in the element-resolved valence electronic structure of Bi_2Se_3, Phys. Rev. B **104**, 245105 (2021).

[52] H. Plank, J. Pernul, S. Gebert, S. N. Danilov, J. König-Otto, S. Winnerl, M. Lanius, J. Kampmeier, G. Mussler, I. Aguilera, D. Grützmacher, and S. D. Ganichev, Infrared/terahertz spectra of the photogalvanic effect in (Bi,Sb)Te based three-dimensional topological insulators, Phys. Rev. Mater. **2**, 024202 (2018).

[53] I. Mohelsky, J. Wyzula, F. Le Mardelé, F. Abadizaman, O. Caha, A. Dubroka, X. D. Sun, C. W. Cho, B. A. Piot, M. F. Tanzim, I. Aguilera, G. Bauer, G. Springholz, and M. Orlita, Electronic band structure of Sb_2Te_3, Phys. Rev. B **109**, 165205 (2024).

[54] I. A. Nechaev, I. Aguilera, V. De Renzi, A. di Bona, A. Lodi Rizzini, A. M. Mio, G. Nicotra, A. Politano, S. Scalese, Z. S. Aliev, M. B. Babanly, C. Friedrich, S. Blügel, and E. V. Chulkov, Quasiparticle spectrum and plasmonic excitations in the topological insulator Sb_2Te_3, Phys. Rev. B **91**, 245123 (2015).

[55] M. Battiato, I. Aguilera, and J. Sánchez-Barriga, Generalized GW+Boltzmann approach for the description of ultrafast electron dynamics in topological insulators, Materials **10**, 810 (2017).

[56] G. Pizzi, V. Vitale, R. Arita, S. Blügel, F. Freimuth, G. Géranton, M. Gibertini, D. Gresch, C. Johnson, T. Koretsune *et al.*, Wannier90 as a community code: New features and applications, J. Phys.: Condens. Matter **32**, 165902 (2020).

[57] For representing the Wannier functions in real-space a calculation without SOC was used, as these plots in the presence of SOC are not implemented in the SPEX code yet. However, it is expected that the SOC will have a very small effect on the shape of these Wannier functions.

[58] D. Takane, S. Souma, T. Sato, T. Takahashi, K. Segawa, and Y. Ando, Work function of bulk-insulating topological insulator $Bi_{2-x}Sb_xTe_{3-y}Se_y$, Appl. Phys. Lett. **109**, 091601 (2016).

[59] B. Ryu, Work function of bismuth telluride: First-principles approach, J. Korean Phys. Soc. **72**, 122 (2018).

[60] K. Gundlach, Zur Berechnung des tunnelstroms durch eine trapezförmige Potentialstufe, Solid-State Electron. **9**, 949 (1966).

[61] G. Binnig, K. H. Frank, H. Fuchs, N. Garcia, B. Reihl, H. Rohrer, F. Salvan, and A. R. Williams, Tunneling spectroscopy and inverse photoemission: Image and field states, Phys. Rev. Lett. **55**, 991 (1985).

[62] H.-S. Huang, W.-Y. Chan, W.-B. Su, G. Hoffmann, and C.-S. Chang, Measurement of work function difference between Pb/Si(111) and Pb/Ge/Si(111) by high-order Gundlach oscillation, J. Appl. Phys. **114**, 214308 (2013).

[63] D. Yildiz, M. Kisiel, U. Gysin, O. Gürlü, and E. Meyer, Mechanical dissipation via image potential states on a topological insulator surface, Nat. Mater. **18**, 1201 (2019).

[64] S. Blügel, Theorie der Rastertunnelmikroskopie, in *Physik der Nanostrukturen*, Band 01 (Verlag des Forschungszentrums Jülich, Jülich, 1998), Chap. A3, pp. A3.1–A3.56.

[65] G. Mándi and K. Palotás, Chen's derivative rule revisited: Role of tip-orbital interference in STM, Phys. Rev. B **91**, 165406 (2015).

[66] An approach similar to the method presented here for calculating the tunneling current is known as the revised Chen's derivative rule and described in Ref. [65].

[67] L. Gross, N. Moll, F. Mohn, A. Curioni, G. Meyer, F. Hanke, and M. Persson, High-resolution molecular orbital imaging using a *p*-Wave STM tip, Phys. Rev. Lett. **107**, 086101 (2011).

[68] I. Abilio, N. Néel, J. Kröger, and K. Palotás, Scanning tunneling microscopy using CO-terminated probes with tilted and straight geometries, Phys. Rev. B **110**, 125422 (2024).

[69] N. Oinonen, A. V. Yakutovich, A. Gallardo, M. Ondráček, P. Hapala, and O. Krejčí, Advancing scanning probe microscopy simulations: A decade of development in probe-particle models, Comput. Phys. Commun. **305**, 109341 (2024).

[70] O. Krejčí, P. Hapala, M. Ondráček, and P. Jelínek, Principles and simulations of high-resolution STM imaging with a flexible tip apex, Phys. Rev. B **95**, 045407 (2017).

[71] P. Hapala, R. Temirov, F. S. Tautz, and P. Jelínek, Origin of high-resolution IETS-STM images of organic molecules with functionalized tips, Phys. Rev. Lett. **113**, 226101 (2014).

[72] P. Hapala, G. Kichin, C. Wagner, F. S. Tautz, R. Temirov, and P. Jelínek, Mechanism of high-resolution STM/AFM imaging with functionalized tips, Phys. Rev. B **90**, 085421 (2014).

[73] A. Liebig, A Matlab program for scanning-probe spectroscopy data analysis, Bachelor thesis, Universität Regensburg, 2014.

[74] M. Nurmamat, E. E. Krasovskii, K. Kuroda, M. Ye, K. Miyamoto, M. Nakatake, T. Okuda, H. Namatame, M. Taniguchi, E. V. Chulkov, K. A. Kokh, O. E. Tereshchenko, and A. Kimura, Unoccupied topological surface state in Bi_2Te_2Se, Phys. Rev. B **88**, 081301(R) (2013).

[75] M. Bianchi, D. Guan, S. Bao, J. Mi, B. B. Iversen, P. D. King, and P. Hofmann, Coexistence of the topological state and a two-dimensional electron gas on the surface of Bi_2Se_3, Nat. Commun. **1**, 128 (2010).

[76] N. D. Lang, Spectroscopy of single atoms in the scanning tunneling microscope, Phys. Rev. B **34**, 5947 (1986).

[77] J. A. Stroscio, R. M. Feenstra, and A. P. Fein, Electronic structure of the Si(111)2 × 1 surface by scanning-tunneling microscopy, Phys. Rev. Lett. **57**, 2579 (1986).

[78] R. M. Feenstra, J. A. Stroscio, J. Tersoff, and A. P. Fein, Atom-selective imaging of the GaAs(110) surface, Phys. Rev. Lett. **58**, 1192 (1987).

[79] A. J. Weymouth, T. Wutscher, J. Welker, T. Hofmann, and F. J. Giessibl, Phantom force induced by tunneling current: A characterization on Si(111), Phys. Rev. Lett. **106**, 226801 (2011).

[80] J. Liu and D. Vanderbilt, Topological phase transitions in $(Bi_{1-x}In_x)_2Se_3$ and $(Bi_{1-x}Sb_x)_2Se_3$, Phys. Rev. B **88**, 224202 (2013).

[81] K. Schouteden, Z. Li, T. Chen, F. Song, B. Partoens, C. Van Haesendonck, and K. Park, Moiré superlattices at the topological insulator Bi_2Te_3, Sci. Rep. **6**, 20278 (2016).

[82] P. Cheng, C. Song, T. Zhang, Y. Zhang, Y. Wang, J.-F. Jia, J. Wang, Y. Wang, B.-F. Zhu, X. Chen, X. Ma, K. He, L. Wang, X. Dai, Z. Fang, X. Xie, X.-L. Qi, C.-X. Liu, S.-C. Zhang, and Q.-K. Xue, Landau quantization of topological surface states in Bi_2Se_3, Phys. Rev. Lett. **105**, 076801 (2010).

[83] Y. Jiang, Y. Wang, M. Chen, Z. Li, C. Song, K. He, L. Wang, X. Chen, X. Ma, and Q.-K. Xue, Landau quantization and the thickness limit of topological insulator thin films of Sb_2Te_3, Phys. Rev. Lett. **108**, 016401 (2012).

[84] T. Hanaguri, K. Igarashi, M. Kawamura, H. Takagi, and T. Sasagawa, Momentum-resolved Landau-level spectroscopy of Dirac surface state in Bi_2Se_3, Phys. Rev. B **82**, 081305(R) (2010).

[85] Y. Liu, Y. Y. Li, S. Rajput, D. Gilks, L. Lari, P. L. Galindo, M. Weinert, V. K. Lazarov, and L. Li, Tuning Dirac states by strain in the topological insulator Bi_2Se_3, Nat. Phys. **10**, 294 (2014).

[86] M. Ludewig and G. Chuan Thiang, Cobordism invariance of topological edge-following states, ATMP **26**, 673 (2022).

[87] E. E. Ewert and R. Meyer, Coarse geometry and topological phases, Commun. Math. Phys. **366**, 1069 (2019).